Phase Dynamics and Synchronization of Delay-Coupled Optoelectronic Oscillators

---

A Thesis
Presented to
The Division of Mathematics and Natural Sciences
Reed College

In Partial Fulfillment
of the Requirements for the Degree
Bachelor of Arts

Cristian D. Panda

May 2012

Approved for the Division
(Physics)

Lucas Illing

Acknowledgements

As it often happens in academic research, this work is the result of the collaboration of many brains and hands. I am grateful to the following people:

Lucas, for his support and enthusiasm during the time I have spent in the Nonlinear Optics Lab. I could not have had a better research experience.

John Essick, Joel Franklin, David Griffiths, Mary James, David Latimer, Nelia Mann, Johnny Powell, and Darrell Schroeter, for their advice, dedication and support throughout my years at Reed. I don't remember sitting in a Physics class at Reed I didn't enjoy. Also, Jay Ewing, for his advice and conversations about experimental physics and more.

All of my friends, especially Indu, Jessica, Kritish, Nisma and Tsering, for keeping each other sane and lively during our time at Reed. You are all great and I will miss you.

David Rivera, Dana Bays and the whole International Student Services, for offering me a sense of belonging during my freshman year and throughout my college years.

The Nance family for offering me a home away from home.

My family, for supporting me in everything I do and for their sacrifices.

Mischka for always being there for me. Thank you.

Table of Contents

List of Tables

List of Figures

Abstract

We study experimentally, numerically, and analytically the phase dynamics and synchronization of two nonlinear optoelectronic oscillators with weak time-delayed mutual coupling and strong time-delayed feedback. Three distinct phase dynamic behaviors are observed and analyzed experimentally: in-phase locking, anti-phase locking, and multi-timescale oscillations. In parameter space, the system alternates between these behaviors as a function of the ratio of the coupling delay to feedback delay. We construct a delay differential equations model that simulates the experimental system studied and shows that the observed dynamics can be reproduced numerically for various ranges of parameters. Analytically, we implement a model of Kuramoto phase oscillators and study its solutions and stability. We show that considering just phase-oscillations in our system is sufficient to account for the phase-locking behavior of the two weakly coupled oscillators.

Introduction

My thesis is a study of the phase dynamics and synchronization of delay-coupled nonlinear oscillators. The motivation behind the study of such systems rests in their importance in various fields of science, such as brain dynamics [1, 2], laser arrays [3], population dynamics [4], and optical systems [5, 6]. On a practical level, these systems have numerous potential applications in chaos communication [7, 8], cryptographic key exchange [9], and random number generation [10], to name a few.

While two uncoupled oscillators exhibit uncorrelated behavior, they can become correlated when coupled in the right way, a phenomenon referred to as synchronization or phase-locking. A special case is isochronous synchronization or in-phase oscillations, when the phase shift between the two correlated nonlinearity output signals is zero and they behave identically.

In particular, this thesis focuses on the phase dynamics and synchronization of two nonlinear oscillators with strong feedback, coupled with mismatched weak coupling delays. The underlying topology of the system studied is shown in Fig. 1, where the discs represent identical nonlinear oscillators and the connecting lines represent signals (or information) being transfered between them. The delay parameters τ represent the propagation time along these communication channels. The exchanged signals are amplified by factors γ, which we refer to as coupling strengths. Another important property of our dynamics is that propagating signals are bandpass filtered, which means that their oscillation frequencies are limited by our experimental devices. The interplay of these parameters give rise to very rich dynamics, ranging from steady state solutions and periodic oscillations to chaos.

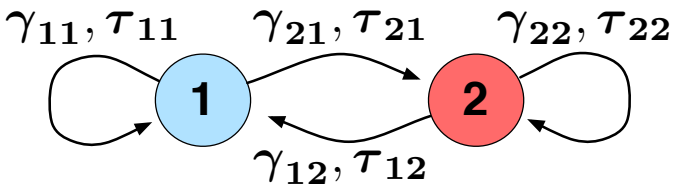

Figure 1: Schematic representation of the network motif studied in this thesis, two coupled nonlinearities with self-feedback.

Our previous research on such systems has focused on the case of equal coupling delays [11], where we are able to predict the emergence of synchronization dynamics using the analytical method of the master stability function (MST). Naturally, the ensuing question we were interested in is the case of mismatched delays. The MST

method is difficult to implement in this case due to the lack of symmetry of the system. Furthermore, while searching for complementary analysis methods, we found the few papers published on the subject [12, 13] difficult to discuss analytically or reproduce experimentally.

Consequently, for unequal delays, we focus on the case of weak-coupling, in regimes close to the onset of periodic oscillations which are easier to analyze. The goals of this thesis are to test whether synchronization is possible when delays are not matched, to study the conditions under which it occurs, and to explain and generalize the behavior of the particular network structure studied to general networks using theoretical analysis and modeling.

Since the observed dynamics are very sensitive to the chosen system parameters, we devote a large portion of our discussion to designing and running an experiment with high precision parameter control that allows us to scan relatively large parameter ranges. Chapters 1-2 detail the experimental apparatus, the different control methods used, and the observed dynamics. In chapter 3, we derive a model for our system and use numerical analysis to deepen our understanding of the experimental results. In chapter 4, we introduce the theoretical phase-model of Kuramoto oscillators and show that the solutions to this model explain the observed dynamics.

Chapter 1

The Experimental Apparatus: Components and Connections

Chapter I is an introduction to the experimental apparatus used in this thesis. In the first part of the chapter, I will discuss the optoelectronic devices used to perform the experiment. The second part of the chapter explains the methods used to implement the delayed coupled networks that are of interests to us, including initial setup, parameter control and selection, and data acquisition.

1.1 Components

1.1.1 Mach-Zehnder Modulator

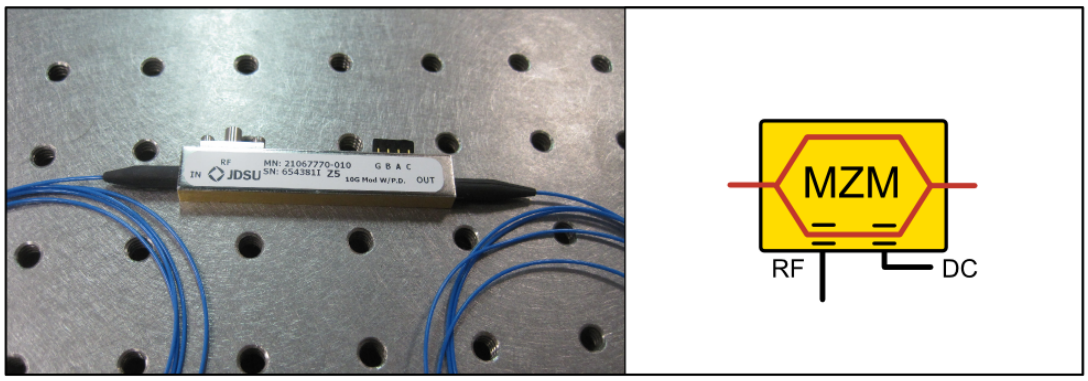

Figure 1.1: Image depicting the Mach-Zehnder Modulator (left) and graphical representation (right). Note the optical input and output ports, and the RF and DC electrical inputs ports in the MZM.

The central device of our system, providing the nonlinear transformation that is responsible for many of the interesting dynamical behaviors in our experimental system, is the $LiNbO_3$ Mach-Zehnder modulator (MZM). The JDSU Z5 MZM is designed for use in telecommunication circuits and operates on the principle of a Mach-Zehnder

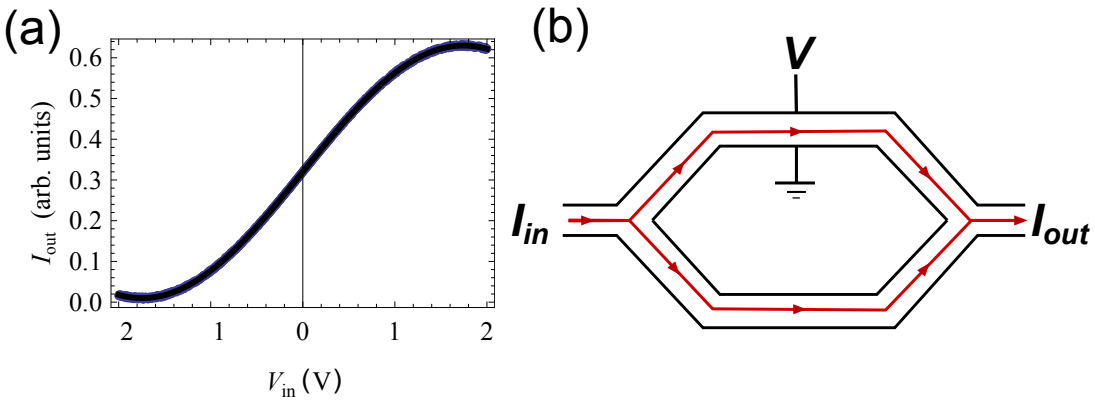

Figure 1.2: **(a)** Experimental data (blue dots) and theoretical prediction (black) of the transfer function of an MZM. Notice that the MZM is biased at the half-transmission point of the transmission curve ($\phi = -\pi/4$) **(b)** Representation of the MZM structure detailing the applied voltage in one of the two paths that the beams travel through.

interferometer. As shown in Fig. 1.2 (b), the incoming light is split into two paths in a ratio depending on the light's polarization[1]. The device exploits the electro-optic effect: a voltage is applied in one of the arms of the $LiNbO_3$ crystal, increasing the index of refraction of the material. Due to the greater index of refraction, light travels at a slower speed in the respective arm of the device. Consequently, a relative phase shift between the two beams proportional to the applied voltage is introduced and when the two beams recombine and interfere, the intensity of the resulting signal is modified.

In order to understand the dynamical behavior of the MZM, we can quantify the interference effect by referring to electromagnetic theory. In our case, the two interfering beams travel in the same direction, have identical polarizations (obtained with the polarizer) and equal amplitudes. For simplicity, consider two plane waves polarized in the x-direction and traveling in the z-direction with a relative phase shift of θ. In complex notation, the plane waves are mathematically described by

$$\tilde{\boldsymbol{E}}_1 = Ee^{i(kz-\omega t)}\hat{\boldsymbol{x}} \quad \text{and} \quad \tilde{\boldsymbol{E}}_2 = Ee^{i(kz-\omega t+\theta)}\hat{\boldsymbol{x}}. \tag{1.1}$$

When the two electric field interfere, the result is a new plane wave

$$\tilde{\boldsymbol{E}}_3 = \tilde{\boldsymbol{E}}_1 + \tilde{\boldsymbol{E}}_2 = E(1+e^{i\theta})e^{i(kz-\omega t)}\hat{\boldsymbol{x}}. \tag{1.2}$$

Using the identity relating the electric field of a plane wave and its intensity [14], we obtain for the intensity of the combined beams

$$I = \frac{1}{2}\epsilon_0 c\,\mathrm{Re}\left[\tilde{\boldsymbol{E}}_3\tilde{\boldsymbol{E}}_3^{\,*}\right] \tag{1.3}$$

$$= \frac{1}{2}\epsilon_0 c[2E^2(1+\cos\theta)] \tag{1.4}$$

$$= 2\epsilon_0 cE^2\sin^2(\theta/2+\pi/2). \tag{1.5}$$

[1]Polarization can be varied using polarization controllers as described in subsection 1.1.3.

Next, we convert Eq. (1.5), describing the behavior of the MZM, to a form that is easily comparable to our system. To that end, we consider how variables E and θ translate to parameters in our experimental setup.

Since laser power is attenuated by the MZM, the irradiance of the output is directly proportional to the input, within a factor of the MZ gain $I_{out} = \gamma I_{in}$. Also, as discussed above, the phase shift θ is proportional to the voltage applied to the crystal, which in our case is a combination of RF (V_{in}) and DC (V_{DC}) signals,

$$\theta = 2b(V_{in} + V_{DC}). \tag{1.6}$$

Here b is a parameter of the system given by $b = \frac{\pi}{2V_\pi}$, where V_π is the DC half-wave voltage. To generalize our result, we add another phase factor ϕ', which gives

$$I_{out} = \gamma I_{in} \sin^2(bV_{in} + bV_{DC} + \phi'). \tag{1.7}$$

Writing the equation with a single phase term $\phi = bV_{DC} + \phi'$, we obtain

$$I_{out} = \gamma I_{in} \sin^2(bV_{in} + \phi). \tag{1.8}$$

In our experiments, V_{DC} is fixed and determines the location of the nonlinearity bias point and V_{in} provides RF modulation. While the JDSU Z5 MZM performs very well experimentally (such as exemplified in the experimental data shown Fig. 1.2(a)), it is important to be aware of some of its limitations. Up to 50 % of input power is lost in the modulator, which can increase the need for amplification in the experimental apparatus. The modulators are temperature-sensitive and we have observed drifting in the biasing of the DC port, which makes their parameters very sensitive and difficult to accurately control.

1.1.2 Laser Diode

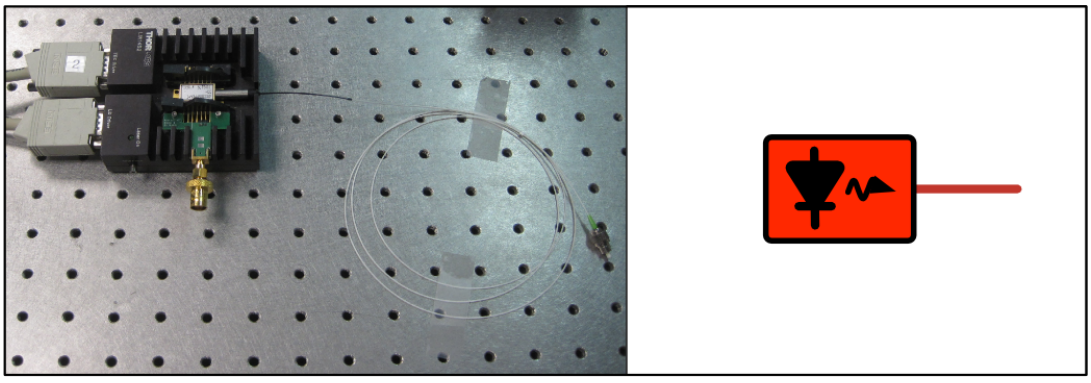

Figure 1.3: Image depicting the fiber coupled laser diode (left) and graphical representation (right). Note the two electrical connectors to the constant temperature and constant current electronic controllers on the left side of the image.

The optical power in our system is provided by a fiber coupled Sumitomo Electric SLT5411-CC laser diode with optical isolator. This continuous-wave semiconductor

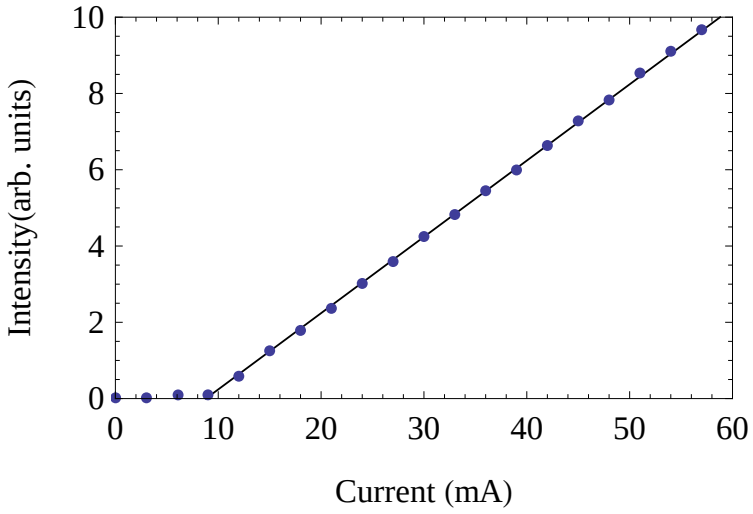

Figure 1.4: Experimental results relating output optical intensity to input current for a Sumitomo SLT5411-CC diode. Blue dots represent data points and the black line is the best fit for the lasing regime.

laser operates at wavelengths of 1.5 μm and powers of up to 50 mW. As depicted in Figure 1.3, the laser is held at constant temperature and constant current by electronic controllers. While the temperature control stabilizes the frequency of the beam, the current control allows us to vary the intensity of the output. The temperature control is rarely varied since the frequency is held constant in our experiments, but the current control is a valuable mean of varying the gain of the experimental apparatus.

In order to understand the behavior of the laser, we have to discuss the physics of lasers. Consider a laser consisting of a cavity with a mirror on one end, a partially transparent mirror at the other end, and a semiconductor gain medium in between. The atoms in the gain medium have two states available: a ground state and an excited state. Atoms can be excited from the ground state to the excited state or they can drop from the excited state to the ground state by either spontaneous emission or stimulated emission, both processes emitting photons of equal energy.

When no pump power is added to the system, the huge majority of the atoms are residing in the ground state and no stimulated emission of photons takes place. In order to generate photons, we pump energy into the gain medium and thus raise the atoms to the excited state. When atoms transition back to the ground state, they emit photons. Although some of the created photons are absorbed by the walls of the cavity, many of them bounce around in the cavity and stimulate the excited atoms to emit more photons in a continuous process. As a macroscopic light-field builds up in the cavity, the laser begins to emit light. More details about the process and a quantitative study of the laser diode can be found in Chris May's thesis [8].

When the number of atoms emitting photons through stimulated emission balances the rate at which atoms are pumped into the excited state, the system reaches equilibrium, often referred to as continuous wave (cw)-lasing. In the lasing state, the cavity outputs a coherent, monochromatic beam of constant intensity. In this regime,

the output light intensity is proportional to the rate at which energy is pumped into the system. We can then explain the linear relationship between current and intensity observed experimentally and depicted in Fig. 1.4.

1.1.3 Polarization Controller

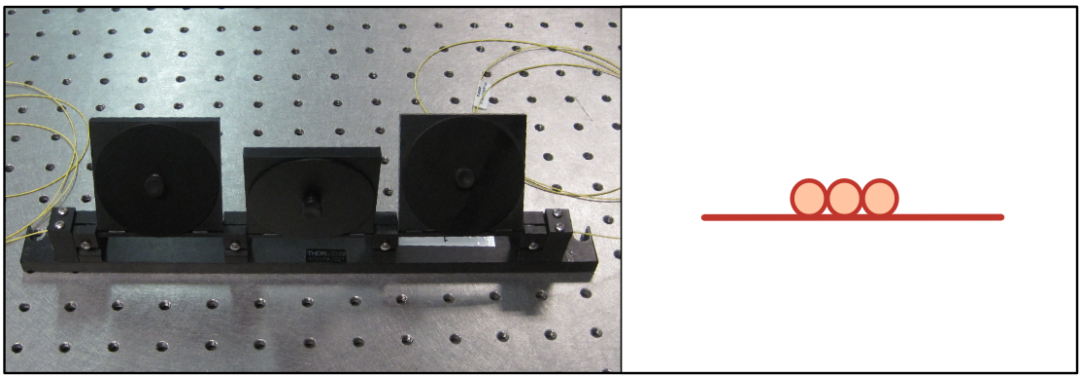

Figure 1.5: Image depicting the polarization controller (left) and graphical representation (right). The three paddles control the orientation of a quarter-wave plate, a half-wave plate and a quarter-wave plate and are used to obtain the suitable polarization for the MZM input.

When light leaves the laser diode, it has some polarization that is dependent on the orientation of the coupled fiber. However, as we have discussed in Section 1.1.1, it is ideal to be able to adjust the polarization of the input light such that the MZM splits the input equally in the two paths, making our analysis in section 1.1.1 valid.

The ThorLabs FPC 560 polarization controller allows us to control the polarization of the light, being able to transform an arbitrary polarization into another arbitrary polarization. It contains three paddles with fiber wound around a cylinder inside of them. The winding results in a well controlled stress of the fiber and thus changes the index of refraction of the fiber in the direction of the stress. Since light polarized in the direction of the stress travels at a different speed than the light polarized in the direction perpendicular to the direction of stress, controlling the number of windings in a paddle allows one to obtain specific relative phase shifts of the output. The paddles are designed to correspond to $\frac{\lambda}{4}$, $\frac{\lambda}{2}$, $\frac{\lambda}{4}$ wave plates, allowing us to vary the polarization of the beam.

Assuming an arbitrary elliptical incident polarization, the first quarter-wave plate is oriented to transform the incident elliptical polarization into linear polarization, then a half-wave plate changes the orientation of the linear polarization, and the second quarter-wave plate transforms the rotated linear polarization into the desired arbitrary elliptical output polarization [15].

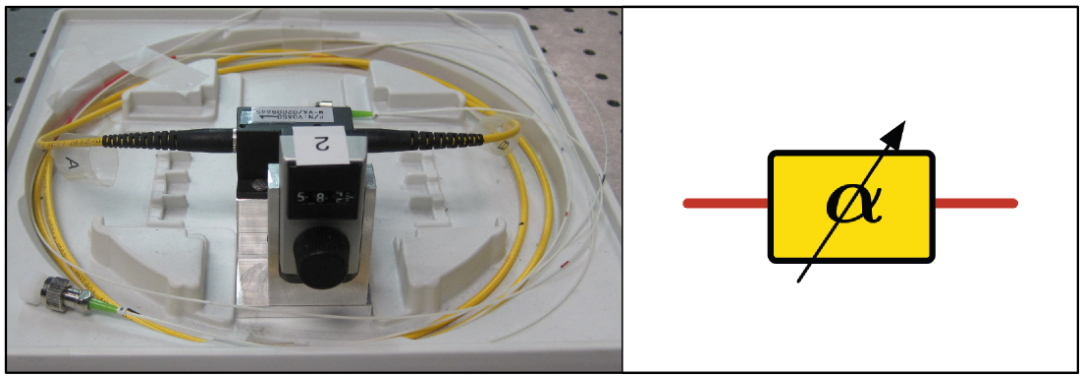

Figure 1.6: Image depicting the adjustable optical attenuator (left) and graphical representation (right). The amplitude of the incoming optical signal can be controlled by using the attached numerical dial.

1.1.4 Optical Attenuator

The ThorLabs VOA-50-APC variable optical attenuator provides a versatile method of controlling the gain of the optical circuit without disconnecting the optoelectronic circuit. The device offers attenuation rates of the power level of an optical signal of up to -50 dB. The attenuators have been equipped with a mechanical dial such as presented in Fig. 1.6. More details about the setup can be found in Greg Hoth's 2010 thesis [16].

The dial directly controls the level of attenuation. The calibration is done by finding the maximum output of the attenuator, scanning the dial range in increments until intensity is reduced to zero and measuring the transmitted intensity as a function of the dial position. We can define an attenuation factor $\alpha = \frac{I_{out}}{I_{max}}$, where I_{out} is the intensity of the output and I_{max} is the maximum intensity of the output for a fixed

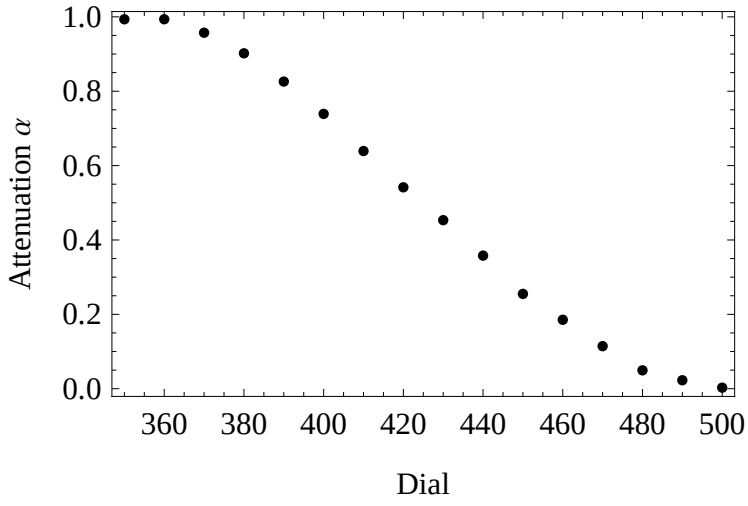

Figure 1.7: Experimentally measured attenuation curve for Thor Labs VOA-50-APC variable optical attenuator.

input. Figure 1.7 depicts an experimentally measured attenuation curve.

1.1.5 Adjustable Optical Fiber Delay Line

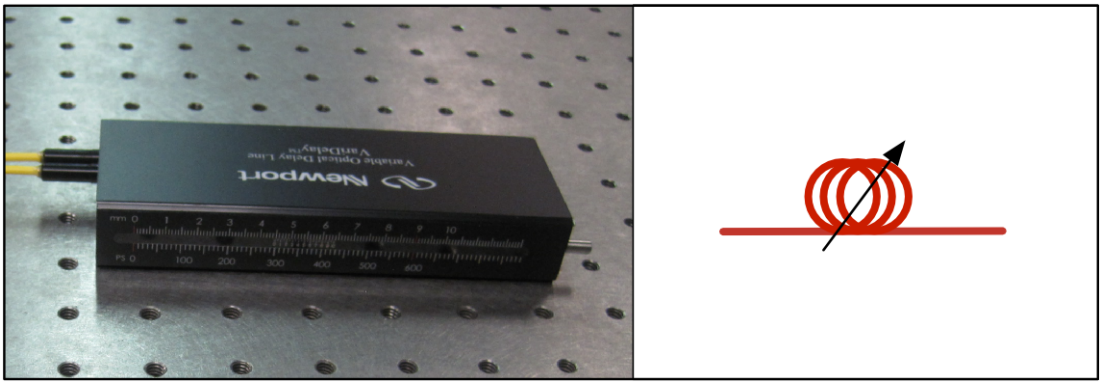

Figure 1.8: Image depicting the adjustable optical delay line (left) and graphical representation (right). The device allows for the delay to be varied within a range of 0-600 ps without disconnecting the apparatus.

The Newport F-VDL-1-6-FA-P variable delay line offers a versatile solution to finely controlling delay times in our circuit. While splicing[2] offers a good solution for the adjustment of large (order of ns) delays, very fine adjustments of up to tens of picoseconds[3] are impossible to obtain using this method.

The adjustable optical fiber delay line is controlled by a mechanical dial over a range of 600 ps and can be adjusted very precisely with the use of the provided Vernier scale. The device functions by finely rotating a crystal with high index of refraction. The distance light travels in the crystal changes with the incident angle and thus the time delay in the circuit is varied.

1.1.6 Optical Splitter and Circulator

The Newport F-CPL-B12355 optical splitter is a relatively straight-forward device. Equipped with three ports, it can split an incoming light beam (I_{in}) into two equal intensity ($I_{in}/2$) beams. The device also works the reverse way, by adding up two input optical signals in a 1:1 ratio.

The device is build such that the two ingoing fibers are physically joined and the beam resulting from the superposition of the input beams is collected in the output fiber line. Loses are generally very low (less than 2% in intensity) and the splitting ratio is very close to the 50/50 ideal value.

The Thorlabs 6015-3-APC optical circulator is a three-port device designed such that light entering into one of the ports is routed to the next port in a circular

[2]Splicing is the technique of joining two fibers together to form a continuous optical waveguide by melting the fiber ends together with an electric arc.

[3]A delay of 10 ps corresponds to 2.2 mm of optical fiber length.

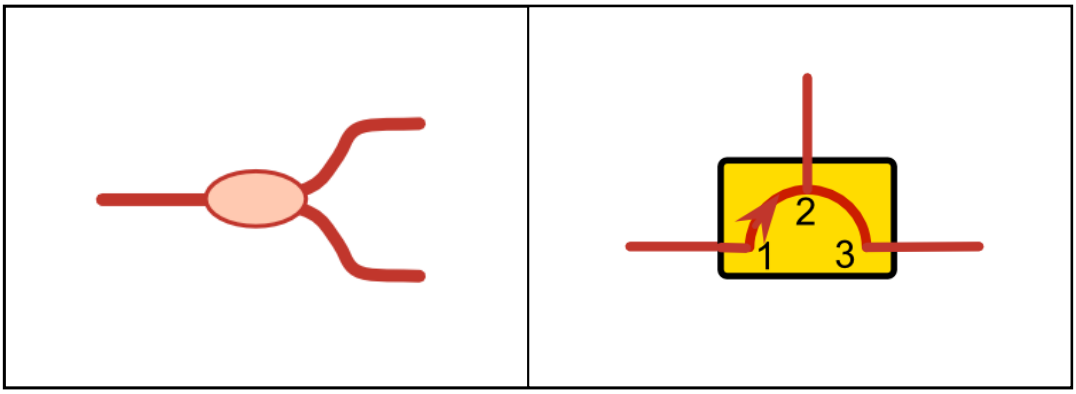

Figure 1.9: Graphical representation of the optical splitter (left) and circulator (right).

manner. Thus, the signal entering port 1 is redirected to port 2 and the signal from port 2 is redirected to port 3. The optical circulator is useful when trying to achieve bi-directional transmission over a single optical fiber. The reasons for designing our system such that beams travel bi-directionally will become clear when we present our experimental design.

1.1.7 Electrical Photodetector, Splitter and Amplifier

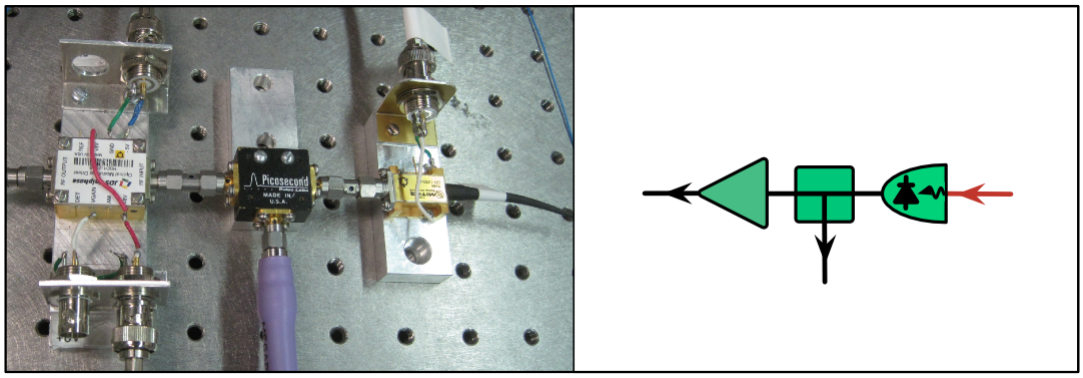

Figure 1.10: Image depicting the three electronic devices in our apparatus. From right to left: photodetector, splitter and amplifier (left) and graphical representation (right). The purpose of the electronic part of the circuit is to convert optical signals to electric signals viewable on an oscilloscope and to amplify the signals in order to compensate for losses.

The electronic components of our system fulfill three very important roles: (1) to convert the optical signal into an electric signal suitable for detection (photodetector), (2) to allow for the measurement of network dynamics by splitting the signal into two equal power signals, one that is measured by an oscilloscope and one that can be returned to the system (splitter) and (3) to amplify the signal to compensate for the signal losses (amplifier). The devices used are a MITEQ DR125-G photodetector with

maximum input power of 3mW, a Picosecond Pulse Labs Model 5331 6dB electrical splitter and a JDSU H 301 power amplifier with a gain of $g_{MD} = -23$.

Another very important feature of these electronic components is that they provide bandpass filtering in the system. The filtering occurs because of the finite response time of the electrical components (low-pass filter) and the fact that they are AC coupled (high-pass filter). The bandwidth limits for each component are presented in Table 1.1. The presence of filtering is extremely important for the dynamical behavior of our system, as will be discussed in Chapter 3.

Table 1.1: Bandwidth limits of the electrical devices in our system.

Electric Device	low-frequency cutoff	high-frequency cutoff
Photodetector	30 kHz	13 GHz
Splitter	0	18 GHz
Amplifier	75 kHz	10 GHz

There are some issues that we should be aware of with the electric devices. First, both the amplifier and photodetector are inverting devices. While this fact does not affect the behavior of our system per se, it is important to acknowledge this detail when measuring certain outputs. For example, when measuring the output of the photodetector, the signal observed is the inversion of the actual optical signal in the circuit. Another issue to be aware of is that the gains of the photodetector and amplifier are constant for low input power, but the components slowly start to saturate at high powers.

1.1.8 Connections

All optical devices are fiber coupled with single mode fiber and FC/APC (Angled Physical Contact) connectors. These connectors can be screwed together using a mechanical plug. Losses in such connections are usually small ($< 5\%$), but should be taken into account for the more sensitive experiments. Back-reflection in the optical connection is minimized by the design of the connectors: they are polished at an angle that minimizes back-reflection.

The electronic devices are connected with wide-bandwidth SMA type connectors that should not affect our dynamics very much. All electric outputs are terminated at 50 Ω in order to prevent back-reflection.

1.2 Data Acquisition: Observing the network dynamics

The main instrument used to observe the dynamics of our experimental network is an Agilent Infiniium DSO81264A fast real time oscilloscope running at sampling rates of up to 40 Gbit/s and detecting frequencies of up to 12 GHz. The oscilloscope is ideal for observing the fast time-series of our signal due to its high bandwidth, comparable to the bandwidth of our electrical filtering. Measuring signals in different parts of our system allows us to determine and compare different dynamics of nodes in our delay-coupled network by analyzing the raw time-series data.

The Picosecond 12050 pattern generator is a second important tool that helps in many of the stages of the experimental system buildup and adjustment. While any signal can be used to adjust the required laser power, attenuation, and MZ bias point (as described in section 1.5); the delay is hard to match without a signal with a very short rise-time. The 12.5 Gbps ultra-fast function generator outputs signals with a 25 ps rise time, allowing us to measure delay mismatches of up to 10 ps. The adjustable pulse train allows us to select the appropriate shape for our experiment.

1.3 The network architecture

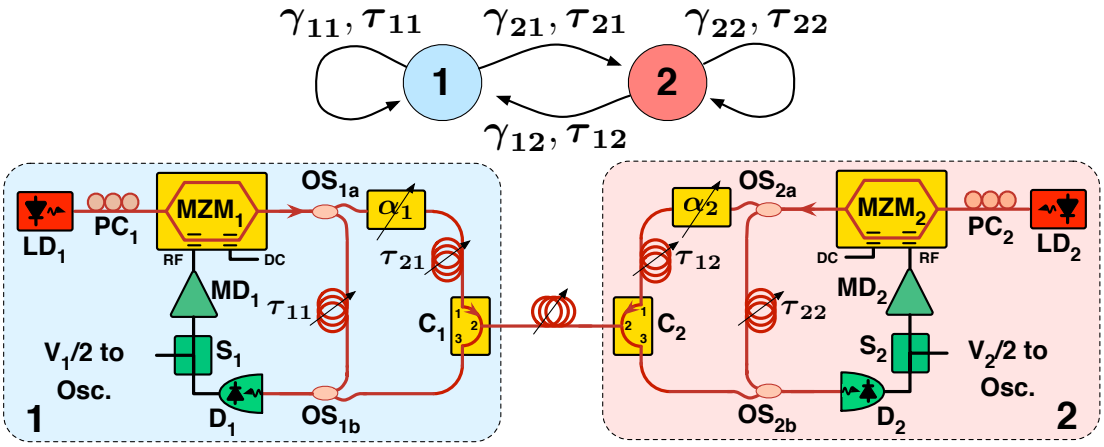

Figure 1.11: Coupling architecture (top) and schematic of the experiment consisting of two coupled optoelectronic oscillators (bottom): LD, laser diodes; PC, polarization controllers; MZM, Mach Zehnder modulators; C, circulators; α, optical attenuators; τ, adjustable delay lines; D, photodetectors; S, electronic splitters; MD, modulator drivers.

Our experimental apparatus is obtained by connecting the individual components discussed above to form to a particular network architecture. The network involves two delay coupled optoelectronic oscillators in a chain configuration, each of them with delayed self-feedback. Each node in our network represents the nonlinearity of our system, the MZM, which is coupled back to itself and to the other system nodes

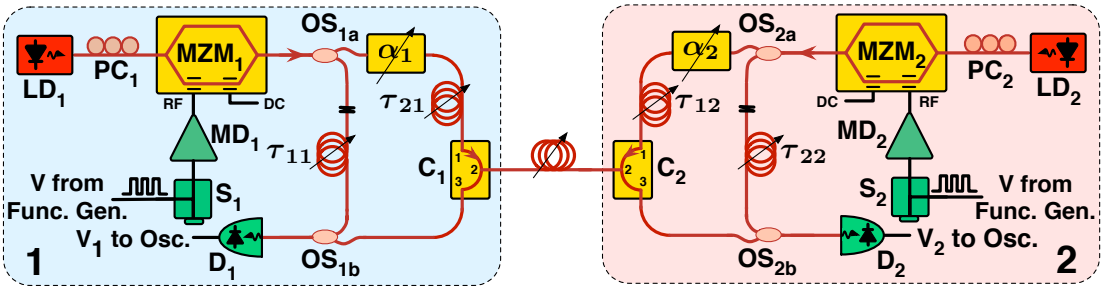

Figure 1.12: Schematic representation of the setup used to measure and match the free parameters of our system. Note the two interrupted optical fiber connections in the self-feedback loops. In this case, the two coupling strengths and delays in the cross-coupling links can be measured and compared. Using this method, but breaking different parts of the circuit, any parameters in the system can be compared.

with optical fiber. For experimental convenience, control network components are added such that system parameters can be matched or varied with maximum ease. The complete experimental setup and coupling network are presented in Figure 1.11.

1.4 Experimental techniques

The main focus of this section is to describe the experimental procedures used to control the system's dynamics. There are four very important parameters that can be adjusted experimentally: the attenuation, laser current, delay and the bias point of the MZM. In order to accomplish this, we disconnect parts of our system as depicted in Figure 1.12, input a square wave signal at the power amplifiers MD_1 and MD_2 and observe the two outputs V_1 and V_2 on the oscilloscope. This versatile setup allows us to set all four free parameters of our system.

1.4.1 Laser Current and Attenuation

Both laser current and attenuation are parameters affecting gain. As observed in Figure 1.11, varying the value of the laser current for each diode will vary both the gain in the corresponding self-feedback loop and the cross-coupling strength[4]. The attenuators are placed in the cross-coupling link, so that the level of attenuation α will only affect the gain in the respective link.

In our case, for symmetry reasons, we want to keep the self-feedback strengths equal ($\gamma_{11} = \gamma_{22} = \gamma_f$) and let coupling strengths be equal ($\gamma_{21} = \gamma_{12} = \gamma_c$), but variable. A good setup for accomplishing these requirements is depicted in Fig. 1.12. By disconnecting either elements in the coupling loop or in the feedback loops, we can have the detectors record the signal propagating through the feedback loop or coupling links respectively, allowing us to measure and set the loop gain.

[4]For example, the current of laser 1 controls γ_{11} and γ_{21}

First, we match the two lasers such that $\gamma_{11} = \gamma_{22} = \gamma_f$. Then, we match the two coupling feedbacks $\gamma_{21} = \gamma_{12} = \gamma_c$ using the two attenuators. Using this procedure, we can scan the range of γ_c relevant to our experiment.

1.4.2 Delay

Since delay is the focus parameter of this thesis, being able to control and measure it with high accuracy and precision is very important. Our goals are (1) to match the two feedback delays $\tau_{11} = \tau_{22} = \tau_f$ and the two coupling delays $\tau_{21} = \tau_{12} = \tau_c$, and (2) be able to easily vary τ_c such that the dynamics of the system can be observed for different ratios of delays τ_c/τ_f.

For accomplishing condition (1), we again use the setup depicted in Fig. 1.12. The signal generator provides a pulse signal input and we simultaneously observe the system outputs on the oscilloscope. Since the lengths of all the BNC cables used are equal, we can compare the times it takes the pulse to travel around each loop and measure the delay difference. By connecting and disconnecting the system as discussed in the earlier subsection, both the coupling delays and feedback delays are matched. An absolute value of each delay can be obtained as well by connecting another BNC cable (same length) to the input splitter and observing the two outputs on the screen.

For large delay mismatches (> 600 ps), we splice cables and insert them into the system to make up for delay difference. For small mismatches (< 600 ps), we use the variable delay lines to adjust the delay. Using this procedure, delays can be matched with 10 ps accuracy.

We also want be able to easily vary τ_c (condition 2) such that the dynamics of the system can be observed for different ratios of delays τ_c/τ_f. This is where the circulators come in handy. In the case of coupling delays, they allow us to transfer optical signal through the same optical fiber bidirectionally. Thus, once delays are matched, we can vary the coupling delay τ_c just by adding another length of fiber to the bidirectional link, which will increase the delay for both coupling links by the same value.

1.4.3 Bias Point of the MZM

For all experiments discussed in this thesis, we bias the MZM to the half-transmission point with a DC-Voltage corresponding to either $\phi = -\pi/4$ or $\phi = \pi/4$. We choose these bias points because the output function of the MZM derived in Eq. (1.8) simplifies greatly in this case [11].

It is important to note that when the bias point is set to $\pi/4$, the small-signal round trip gain is positive and when the bias point is set to $-\pi/4$, the round trip gain is negative. This is of course only true for small signals that cannot explore more than the local slope of the nonlinearity. In our experiment, the distinction between round trip positive and round trip negative gain will prove to be important and will give rise to distinct dynamical behaviors.

The procedure of selecting the $\pm\pi/4$ bias points is the following. First, we find

the maximum intensity of the MZM for a specific signal by varying the DC bias and measuring the output with an inverting photodetector. Then, we adjust the intensity to the point where the output intensity is half the maximum intensity. By probing the region around the bias point, we can decide whether we are on the positive or negative slope. If the output intensity is a monotonically increasing function of the bias voltage, the bias point is $\pi/4$. If the output intensity is a decreasing function of the bias voltage, the bias point is $-\pi/4$.

1.5 Final Thoughts

To summarize, we will be studying the dynamical behavior of a system of two delay-coupled optoelectronic oscillators with self-feedback. Four parameters of the system can be varied: the delay, the laser current, the bias point of the MZ, and the attenuation. Since delay is the parameter of primary interest in this thesis, we will experimentally measure the phase-locking behavior of the two optoelectronic oscillators in the periodic regime for various coupling delays τ_c.

Chapter 2

Experimental Results

In this second chapter, we put to work the designed experimental setup presented in the first chapter. I will start by discussing the motivation behind choosing a specific dynamical regime for our experimental runs, continue by discussing three types of observed dynamical behavior and finish with a discussion of the results in parameter space.

2.1 Discussion of the Chosen Dynamical Regime

Systems of coupled optoelectronic systems exhibit rich dynamical behavior [8, 16–18]. Due to the interplay of the nonlinearity present in our system, filtering effects and the coupling delay, chaotic behavior is observed for large feedback coupling strengths. For lower feedback coupling strengths, many other complex dynamical regimes are observed in our system.

Since the two loop system is, in essence, formed by two identical single loop systems that are coupled weakly, discussing the dynamical regimes of a one loop system accounts for much of the dynamical behavior of the two coupled oscillators. For the single loop system, the various dynamics can be observed by varying the feedback strength while keeping all other parameters fixed. The system exhibits behavior compatible with a classical bifurcation diagram as discussed in Chris May's thesis [8] and presented in Fig. 2.1. As expected, for very weak feedback strengths, the system is in a single steady state, where the power input into the system is insufficient for oscillatory dynamics. As we increase the feedback strength, we observe sinusoidal oscillations created by the interplay of the feedback delay and strong feedback. The amplitude of these oscillations scale nonlinearly with feedback strength [16, 19], but they soon start losing their sinusoidal shape and become square waves. As the feedback is increased even more, the system begins to exhibit chaotic behavior, first in the form of chaotic breathers [18] and later as high-dimensional chaos.

After describing the behavior of systems with equal coupling delays in the high-dimensional chaotic regime with the use of the Master Stability Function (MST) [11], we chose to focus my thesis work on the case where delays are not matched. This system presents new analysis challenges, as the MST method is difficult to adapt for

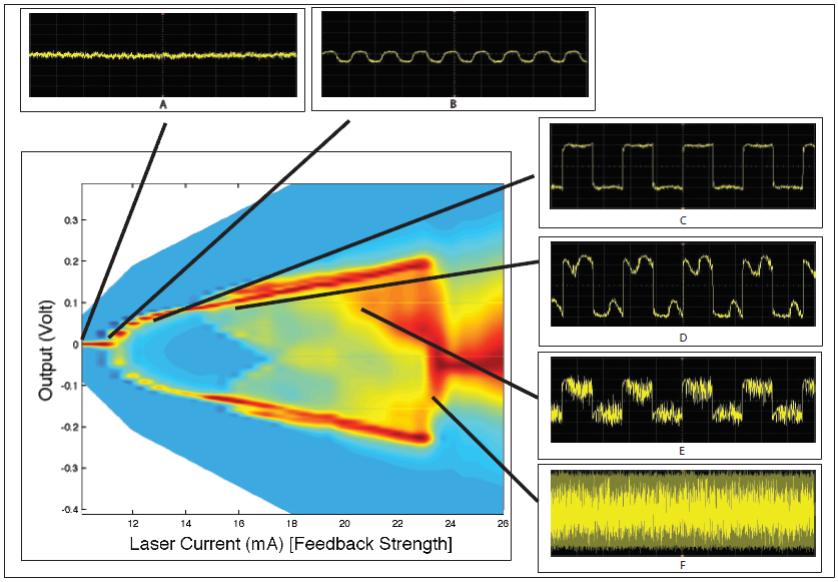

Figure 2.1: Experimentally measured bifurcation diagram of a single loop feedback system. The graph shows a histogram of the observed oscillation amplitudes and is color coded to reflect the normalized distribution of specific oscillatory amplitude, blue representing 0 and red representing 1. Complex transition dynamics, from steady state to periodic oscillations, chaotic breathers and high-dimensional chaos are shown in panels A-F. (*Adapted from [8]).*

unequal delays. Therefore, we have decided to focus on studying the dynamics of our system in the weakly coupled periodic oscillatory regime, when the cross-coupling strengths in the system are low compared to the self-feedback strength and the self-feedback strength is sufficiently low such that chaos is avoided and periodic dynamics are seen. Specifically, we will be studying the synchronization behaviors of two delay-coupled oscillators. Our goal is to understand the mechanisms and conditions that lead to synchronization in our system.

2.2 Observing the Network Dynamics

2.2.1 Running The Experiment

The system is designed so that it is easy for us to observe and compare the dynamics of the two nodes of our network. Using the procedures of section 1.5., we start with the system with the coupling delays matched to $\tau_c = 98.37$ ns and feedback delays matched to $\tau_f = 54.65$ ns. The attenuators and laser powers are set such that the coupling loops are at equal gains and the observed dynamics are in the periodic regime. We bias each MZM to either $\pi/4$ or $-\pi/4$, as desired. By disconnecting the system at the coupling loop[1], we are able to observe the dynamics of the individual

[1]For example, disconnect the coupling variable delay from the circulator.

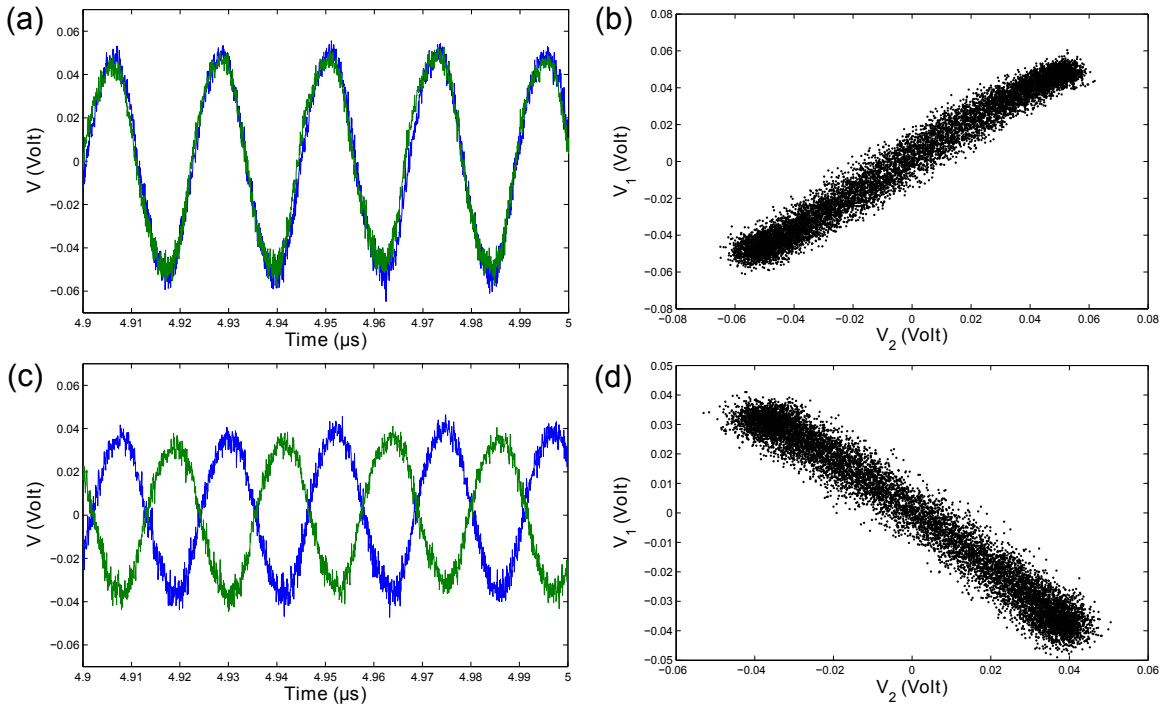

Figure 2.2: Examples of experimentally measured time series (a), (c) and V_1 vs V_2 plots (b), (d) for the two oscillators: Oscillator 1 (blue line), Oscillator 2 (green line). (a),(b) In-phase oscillations and (c),(d) Anti-phase oscillations are exemplified in the figures. The MZMs are biased at $-\pi/4$ for a negative round trip gain.

oscillators separately. If all the parameters are matched, we observe two identical sinusoidal waves with equal amplitudes and periods that are not phase-locked. The two waves wander along the screen and the phase difference between the two signals varies linearly with time.

2.2.2 Types of Correlated Oscillations

While the case of positive round-trip gain ($\phi = \pi/4$) and negative round-trip gain ($\phi = -\pi/4$) both exhibit oscillatory dynamics, it is important to notice that their oscillation frequencies are very different. When the MZMs are biased at $\pi/4$, the frequency of oscillations is observed to be 217 kHz. In contrast, when biased at $-\pi/4$, the frequency of oscillations is 44 MHz. By comparing our oscillations period with the delay, it is clear that the dynamics of the oscillators for the negative round trip gain with period 22.3 ns is on the timescale of the delay $\tau_f = 54.65$ ns, while for positive round trip gain, the timescale of the dynamics with period 4.6 μs is much greater than the timescale of the delay $\tau_f = 54.65$ ns. Therefore, we expect that coupling the two oscillators with delays comparative in length to the self-feedback delay will produce very different synchronization dynamics for the positive and negative gain cases. Therefore, we study the cases when the MZMs are biased at $\phi = \pi/4$ and

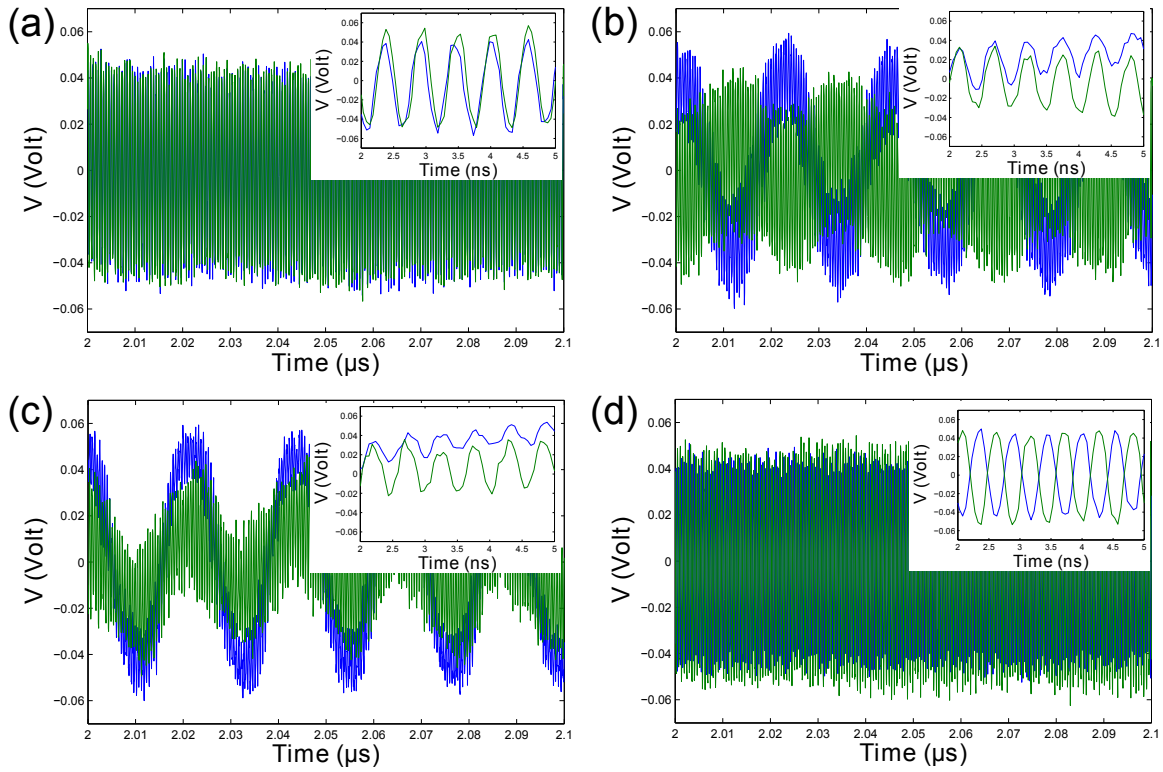

Figure 2.3: Examples of experimentally measured multiple-timescale behavior for Oscillator 1 (blue line) and Oscillator 2 (green line) with the MZMs biased at $-\pi/4$ for a negative round trip gain. (Inset) The same time-series are plotted on a zoomed in time axis (ns range), where very fast GHz range oscillations are observed.

$\phi = -\pi/4$ separately. Since we are interested in the phase behavior of the two weakly coupled oscillators, we can reconnect the system and observe the resulting dynamics.

For the case when $\phi = -\pi/4$, the two coupled nominally identical oscillators synchronize either in-phase or anti-phase, or they exhibit unsynchronized behavior. In the parameter range experimentally probed, three types of network dynamics are observed: in-phase oscillations, anti-phase oscillations, and mutiple-timescale oscillations. The latter corresponds to cases where the dynamics consists of very fast oscillations that sometimes emerge on top of the previously observed slower dynamics.

In-phase oscillations occur when the wave-trains of the two oscillators align. Anti-phase oscillations occur when the wave-trains of the two oscillators are correlated, but with a π phase difference. Figure 2.2 presents acquired data exemplifying the two behaviors for negative round trip gain. In the first plot, the two MZMs oscillate in a correlated fashion, with matched phases and amplitudes. This is exemplified in Fig. 2.2 (b), where we have plotted the voltage of oscillator 1 versus the voltage of oscillator 2. In this case, the diagonal line with slope 1 indicates that the two measured signals are identical at any moment in time. The same analysis is done in Fig. 2.2 (d) for the case of anti-phase oscillations, where the diagonal line with slope

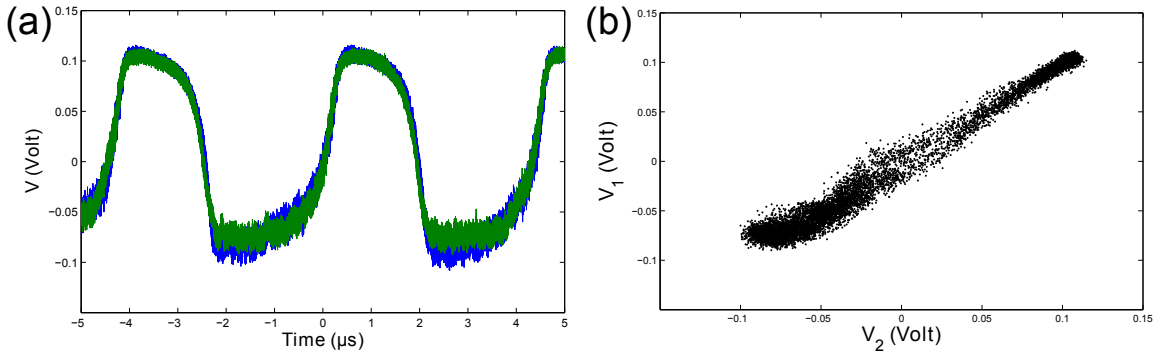

Figure 2.4: Example of experimentally measured time series (a) and V_1 vs V_2 plot (b) for the two oscillators: Oscillator 1 (blue line), Oscillator 2 (green line). The results are consistent with in-phase oscillations. The MZM is biased at $+\frac{\pi}{4}$ for a positive round trip gain.

-1 indicates that the two measured signals are opposite to each other.

Multiple-timescale dynamics occur when new oscillations at a much faster timescale than the ones observed in the synchronization regimes emerge. Experimentally, multiple-timescale behavior is observed as distortions of the original periodic signal. Various examples of observed multiple-timescale dynamics are shown in Fig. 2.3. In Fig. 2.3 (a) and (d), we solely observe very fast oscillations with frequencies on the order of 2 GHz. In this case, the weak coupling between the oscillators introduces instability to the in-phase and anti-phase solutions observed earlier, which are replaced by in-phase and anti-phase very fast oscillations. Figures 2.3 (b) and (c) present cases when weakly coupling the two oscillators does not entirely eliminate the single loop oscillatory dynamics. The new, very fast oscillations are superimposed on previous dynamics, which can be either in-phase or anti-phase depending on the system parameters chosen. While studying in detail the multiple-timescale dynamics presents difficulties due to the variety of the oscillatory regimes available, we see that the two oscillators do no exhibit phase-locking at the timescale associated with the self-feedback delay τ_f.

For the case when the MZMs are biased at $\phi = \pi/4$, the two oscillators are always observed to synchronize in phase for the parameter range experimentally probed, with the oscillation regime pictured in Fig. 2.4. Plotting the voltage of oscillator 1 versus the voltage of oscillator 2 results in a diagonal line with slope 1, showing the in-phase behavior of the two oscillators. As mentioned in the previous section, the period of the observed dynamics is 4.6 μs, much greater than the timescale of the feedback delay $\tau_f = 54.65$ ns.

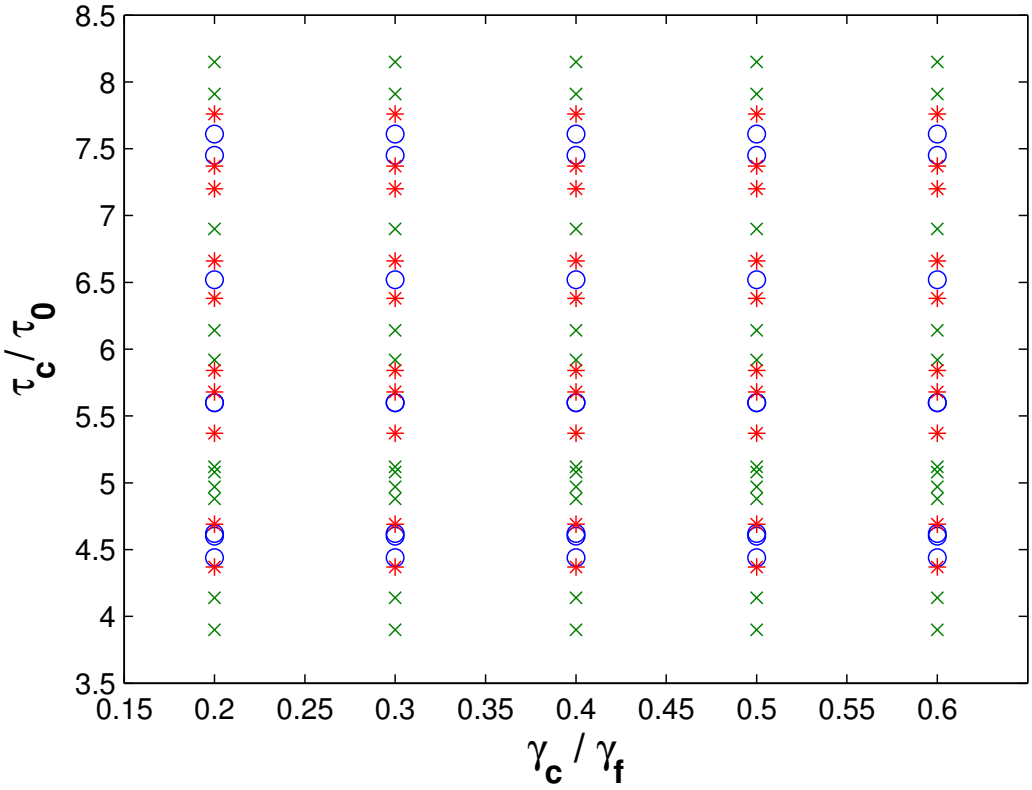

Figure 2.5: Parameter space results depicting phase locking behavior for the case when our oscillators are biased at $\phi - \pi/4$. The two nodes can oscillate in-phase ($\bigcirc$), anti-phase ($\times$) or in the multiple-timescale regime ($*$). Locking bands are observed at $\tau_c/\tau_0 = \{4.5; 5.5; 6.5; 7.5\}$ for in-phase locking and at $\tau_c/\tau_0 = \{4; 5; 6; 7; 8\}$ for anti-phase locking.

2.3 Results in Parameter Space and Discussion

As noted earlier, we are interested in the role of delay and coupling strength in the locking behavior of systems of coupled oscillators. Therefore, we scan the parameter space by varying the coupling delay and strength with fixed feedback delay τ_f = 54.65 ns and strength, and we look for synchronization dynamics. As before, the experiments show two different synchronization dynamics for the cases when we bias the MZMs to $\phi = \pi/4$ and $\phi = -\pi/4$.

2.3.1 Negative Round Trip Gain

For the case of negative round trip gain ($\phi = -\pi/4$), the experimental results obtained are shown in the parameter space plot of Fig. 2.5. We plot on the horizontal axis the cross-coupling strength (γ_c) as a percentage of the feedback strength (γ_f). On the vertical axis, we plot the ratio of the coupling delay (τ_c) to the natural period of the observed uncoupled oscillations τ_0 =22.3 ns. To each experimentally probed location on the parameter plot, we assign a symbol representing one of the types of

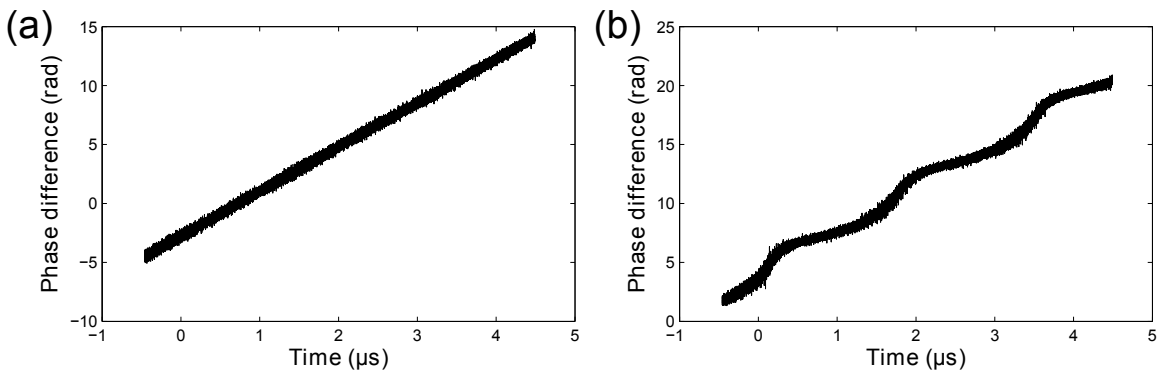

Figure 2.6: Diagrams showing the time evolution of the phase difference between the two oscillators for the case of uncoupled oscillators (a) and very weak coupling (b). Plot (a) displays totally uncorrelated behavior, with each the two oscillators oscillating independently of the other, while plot (b) shows very weakly coupled dynamics, where the two oscillators tend to synchronize (the horizontal plateaus), but are kicked back to the uncoupled mode by noise and parameter mismatch (the constant positive slope).

dynamical behavior observed and presented in section 2.2.2. Therefore, we observe in-phase oscillations ($\bigcirc$), anti-phase oscillations ($\times$) and multiple-timescale oscillations ($*$). The experimental results suggest a very robust system, where all of the observed dynamics falls into one of the categories discussed in section 2.2.2. We do not observe cases where the system oscillates between synchronization and multiple-timescale dynamics. As a general rule, we consider very fast dynamics on GHz scale as indicators of multiple-timescale behavior and always put a red asterisk ($*$) in parameter plot for those cases.

While the experimental data is not sufficient for obtaining a fine resolution description of the system parameter space, the main features are clearly distinguishable. We observe the presence of horizontal alternating in-phase, anti-phase locking and multiple-timescale oscillations bands. The horizontal bands show that the observed dynamical regimes vary with coupling delay τ_c, while they seem to be independent of coupling strength γ_c. Closely examining the correlation between the synchronization bands and the delay ratios on the vertical axis, we observe that two MZMs oscillate in-phase when the ratio of the coupling delay to the natural delay parameters is a half-integer number

$$\frac{\tau_c}{\tau_0} = \frac{2k+1}{2} \qquad \text{(in-phase)}, \tag{2.1}$$

where $k \in \mathbb{Z}$. Similarly, anti-phase oscillations occur when the ratio of the coupling delay to the self-feedback delay is an integer

$$\frac{\tau_c}{\tau_0} = k \qquad \text{(anti-phase)}, \tag{2.2}$$

where $k \in \mathbb{Z}$. Multiple-timescale bands are observed in the regions between the locking bands.

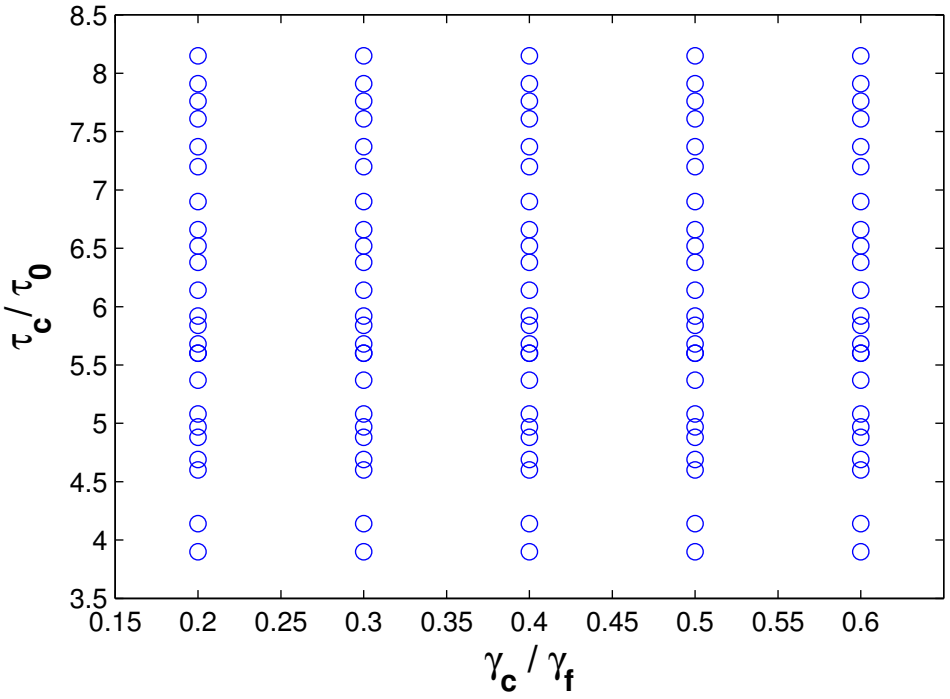

Figure 2.7: Parameter space results depicting phase locking behavior for the case when our oscillators are biased at $\phi = \pi/4$. The two nodes are always observed to oscillate in-phase (○).

In the range experimentally probed, i.e. $0.2 < \gamma_c/\gamma_f < 0.6$, the results show that the strength of the coupling feedback does not affect the locking dynamics of the system in a major fashion. However, since the noise and mismatch in the system introduce instability to the locked oscillatory solutions, very small coupling strengths ($\gamma_c/\gamma_f < 20\%$) are found to be insufficient for maintaining phase-locked dynamics between the two nodes. In these cases, we observe phase slipping, characterized by a tendency of the oscillators to switch between the coupled and uncoupled states or, for extremely weak coupling, be uncorrelated. The two behaviors are shown in Fig. 2.6. In plotting the two graphs, we assume that the two waveforms remain similar, calculate the phase of each oscillator as a function of time and then plot the difference of the two phases. Of course, in the case of stronger coupling, the variations in amplitude induce waveform mismatches and this kind of analysis breaks down, but we will not worry about that at the moment. To interpret the figures, note that, if phase-locked, the phase difference would be a constant and we would plot a horizontal line. When uncoupled, as shown in Fig. 2.6 (a), the two oscillators have a linearly increasing phase difference, indicative of the two oscillators' independent slightly mismatched natural oscillation frequencies. The phase slipping regime, shown in Fig 2.6 (b) is a mixture of the two, with regions where the oscillators synchronize (horizontal plateaus) and regions where the oscillators return to the uncoupled behavior (increasing phase difference).

2.3.2 Positive Round Trip Gain

When the MZMs are biased for the positive round-trip gain at $\phi = \pi/4$, we always observe in-phase locking when scanning the parameter space in the same region as for the $\phi = -\pi/4$ case. In this case, the ratio of coupling delay τ_c to natural period τ_0 does not affect the synchronization dynamics. As discussed in section 2.2.2, the large time-scale of oscillations with a period of 4.6 μs suggests that the system delays τ_c and τ_f do not influence the observed dynamics. As for the negative gain case, for small coupling strengths ($\gamma_c/\gamma_f < 10\%$), the oscillators decouple and we again observe phase slipping behaviors. Unlike in the $\phi = -\pi/4$ case, an analysis of the phase slipping behavior is difficult because of the large timescale of the oscillations. The limited number of oscillations available for data acquisition makes the phase analysis presented in section 2.3.1. very hard to perform.

Chapter 3

Theoretical Model and Numerics

This chapter presents numerical work used to study our system. We begin by developing a model for the system of coupled oscillators with feedback and then use this model for numerical simulations.

3.1 Single oscillator with self-feedback

A good starting point for the theoretical treatment of our systems is the single oscillator with feedback system [17, 20]. In this system, the broadband amplifier is the main device responsible for the dynamical behavior. It is characterized by a high cutoff frequency ω_H, low cutoff frequency ω_L, and gain p. The most convenient way to describe the frequency domain behavior of the filter is the second order bandpass filter shown in Fig. 3.1 with the transfer function

$$H(\omega) = \frac{p}{\left(1 + \frac{1}{i\omega/\omega_L}\right)(1 + i\omega/\omega_H)}. \tag{3.1}$$

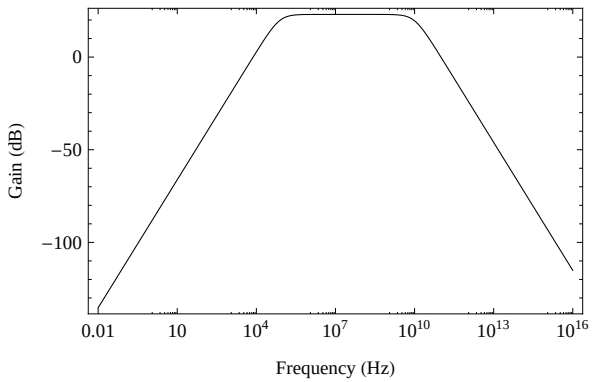

Figure 3.1: Gain (absolute value of transfer function) of the bandpass filter modeling the dynamical behavior in our system measured in dB. Note the logarithmic frequency axis.

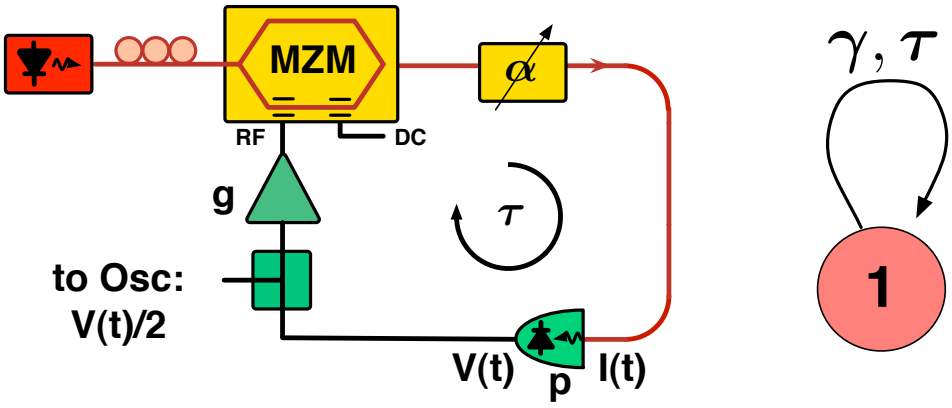

Figure 3.2: (left) Diagram of the single oscillator with self-feedback, indicating the parameters that affect the observed dynamics and coupling architecture. (right) Schematic of the single oscillator with self-feedback.

In order to go forward, we refer to the architecture of our system, presented in detail with parameters that affect the observed dynamics in Fig. 3.2. Succinctly, the photodetector is characterized by the low cut off frequency ω_L, high cut off frequency ω_H and gain p; as discussed in chapter 1, the commercial MZM is characterized by the equation $I = a\sin^2(bV + \phi)$, where V is the voltage input of the MZM and a, b and ϕ are parameters of the device; the amplifier introduces an additional gain factor g. Three parameters, the intensity input to the photodetector $I(t)$, the voltage output of the detector ($V(t)$), and the feedback delay τ, will prove to be important in our derivation.

Now, having defined the relevant quantities in our system, we will be developing a model that allows us to numerically compute the measured signal $V(t)$. Using the definition of the transfer function

$$H(\omega) = \frac{V(\omega)}{I(\omega)}, \tag{3.2}$$

where $V(\omega)$ and $I(\omega)$ are, respectively, the Fourier transforms of the output voltage $V(t)$ and optical intensity input $I(t)$ to the photodiode, we obtain

$$\frac{V(\omega)}{I(\omega)} = \frac{p}{\left(1 + \frac{1}{i\omega/\omega_L}\right)(1 + i\omega/\omega_H)}. \tag{3.3}$$

Expanding Eq. (3.3), we obtain

$$\left(1 + \frac{\omega_L}{\omega_H}\right)V(\omega) + \frac{i\omega V(\omega)}{\omega_H} + \frac{\omega_L}{i\omega}V(\omega) = pI(\omega). \tag{3.4}$$

Now, we transform Eq. (3.4) to the time domain by using the inverse Fourier substitutions $i\omega \to \frac{d}{dt}$ and $\frac{1}{i\omega} \to \int_0^t dt$ to obtain:

$$\left(1 + \frac{\omega_L}{\omega_H}\right)V(t) + \frac{1}{\omega_H}\frac{d}{dt}V(t) + \omega_L\int_0^t V(u)du = pI(t). \tag{3.5}$$

We need to write $I(t)$ as a function of the parameters of the system. Looking at Fig. 3.2, we can see that $I(t)$ is the output of the MZM reduced by the gain factor α. Thus, we obtain $I(t) = \alpha a \sin^2(bv_{in} + \phi)$, where v_{in} is a dimensionless quantity proportional to the signal in the electronic feedback driving the MZM. The signal propagates around the loop in time τ that is proportional to the length of the delay cable $\tau = \frac{nL}{c}$, where n is the index of refraction of the optical fiber, L is the length of the fiber and c is the speed of light in vacuum. Since v_{in} is just the output signal of the MZM a period ago, we have $v_{in} = \frac{1}{2}gV(t-\tau)$, with factors 1/2 and g due to the splitter and amplifier, respectively. Then, we obtain for the intensity of the optical signal $I(t) = \alpha a \sin^2(\frac{1}{2}bgV(t-\tau) + \phi)$. Plugging this into Eq. (3.5), we obtain:

$$\left(1 + \frac{\omega_L}{\omega_H}\right) V(t) + \frac{1}{\omega_H}\frac{d}{dt}V(t) + \omega_L \int_0^t V(u)du = p\alpha a \sin^2(\frac{1}{2}bgV(t-\tau) + \phi). \quad (3.6)$$

It is mathematically convenient to write Eq. (3.6) into a system of two first order delay differential equations (DDEs). To do this, first define the dimensionless variable $x = \frac{1}{2}bgV$ and parameter $\beta = \frac{1}{2}\frac{\omega_H}{\omega_H+\omega_L}bgpa$. Then Eq. (3.6) becomes

$$\frac{\dot{x}}{\omega_H + \omega_L} = -x - \frac{\omega_H\omega_L}{\omega_H + \omega_L}\int_0^t x(u)du + \beta\alpha \sin^2(x(t-\tau) + \phi). \quad (3.7)$$

Now if we define a new variable

$$y = -\frac{\omega_H\omega_L}{\omega_H + \omega_L}\int_0^t x(u)du, \quad (3.8)$$

we observe that its time derivative is just

$$\dot{y} = -\frac{\omega_H\omega_L}{\omega_H + \omega_L}x \quad (3.9)$$

If we also introduce dimensionless time $\bar{t} = t(\omega_H + \omega_L)$, Eq. (3.7) and Eq. (3.9) can be written as

$$y' = -rx \quad (3.10a)$$
$$x' = -x + y + \beta\alpha \sin^2(x(\bar{t} - \bar{\tau}) + \phi) \quad (3.10b)$$

where the prime denotes differentiation with respect to the dimensionless time $\bar{t}$, $r = \frac{\omega_L\omega_H}{(\omega_L+\omega_H)^2}$, and $\bar{\tau} = \tau(\omega_H + \omega_L)$.

3.2 Coupled oscillators with feedback

Now we can run the same argument for the system we are studying, the two coupled oscillators with feedback. As before, we assume that the two photodetectors in our system are the sources of band pass filtering and that the transfer function of each photodetector is given by Eq. (3.1). In Fig. 3.3, the schematic of the cross coupled

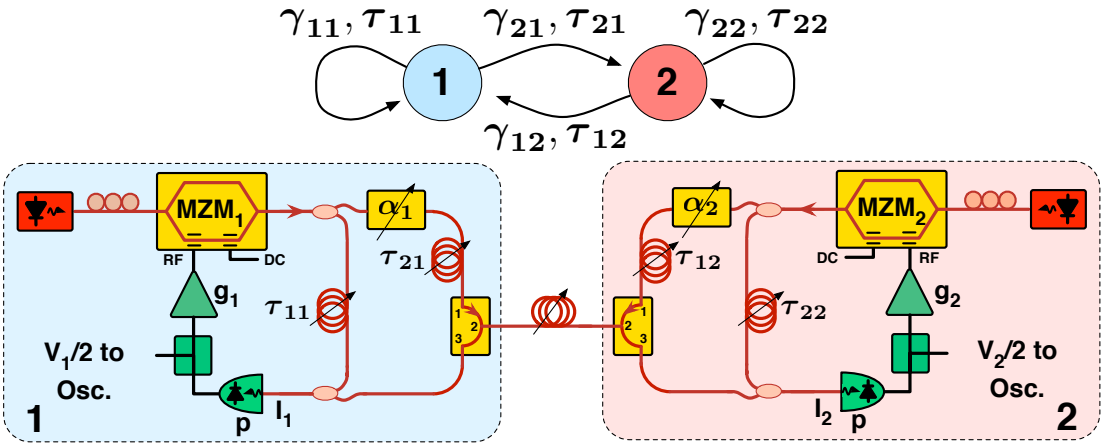

Figure 3.3: Diagram of the single cross-coupled system with self-feedback, indicating the parameters that affect the observed dynamics and coupling architecture.

system with feedback is shown with each component labeled with its characteristic parameters.

Following the same argument as for the single loop system, we obtain for the voltage V_1:

$$\left(1+\frac{\omega_L}{\omega_H}\right)V_1(t)+\frac{1}{\omega_H}\frac{d}{dt}V_1(t)+\omega_L\int_0^t V_1(u)du=pI_1(t), \tag{3.11}$$

where $I_1(t)$ is the intensity input of photodetector 1. Following the diagram shown in Fig. 3.3, we can immediately see that

$$I_1(t)=p\left[\alpha_2 a_2\sin^2\left(\frac{1}{2}b_2g_2V_2(t-\tau_{12})+\phi_2\right)+a_1\sin^2\left(\frac{1}{2}b_1g_1V_1(t-\tau_{11})+\phi_1\right)\right]. \tag{3.12}$$

Since the system is symmetric, the equation for V_2 can be obtained just by switching indices:

$$\left(1+\frac{\omega_L}{\omega_H}\right)V_2(t)+\frac{1}{\omega_H}\frac{d}{dt}V_2(t)+\omega_L\int_0^t V_2(u)du=pI_2(t), \tag{3.13}$$

with I_2 obtained in a similar way to I_1

$$I_2(t)=p\left[\alpha_1 a_1\sin^2\left(\frac{1}{2}b_1g_1V_1(t-\tau_{21})+\phi_1\right)+a_2\sin^2\left(\frac{1}{2}b_2g_2V_2(t-\tau_{22})+\phi_2\right)\right]. \tag{3.14}$$

Since the two oscillators have been experimentally observed to behave identically, we can eliminate the indices $a_1=a_2=a$, $b_1=b_2=b$. Now, in order to obtain a more tractable form of Eq. (3.11) and (3.13), we introduce the dimensionless variables $x_1=\frac{1}{2}b_1g_1V_1$ and $x_2=\frac{1}{2}b_2g_2V_2$, we define $\beta_1=\frac{1}{2}\frac{\omega_H}{\omega_H+\omega_L}pabg_1$ and, $\beta_2=\frac{1}{2}\frac{\omega_H}{\omega_H+\omega_L}pabg_2$

and switch to dimensionless time $\bar{t} = t(\omega_H + \omega_L)$. Equations (3.11) and (3.13) become

$$x_1 + x_1' + \frac{\omega_H\omega_L}{\omega_H + \omega_L}\int_0^t x_1(u)du = \beta_1[\alpha_2 \sin^2(x_2(\bar{t} - \bar{\tau_{12}}) + \phi_2) + \sin^2(x_1(\bar{t} - \bar{\tau_{11}}) + \phi_1)] \tag{3.15a}$$

$$x_2 + x_2' + \frac{\omega_H\omega_L}{\omega_H + \omega_L}\int_0^t x_2(u)du = \beta_2[\alpha_1 \sin^2(x_1(\bar{t} - \bar{\tau_{21}}) + \phi_1) + \sin^2(x_2(\bar{t} - \bar{\tau_{22}}) + \phi_2)] \tag{3.15b}$$

where the prime denotes differentiation with respect to the new dimensionless time.

Finally, defining variables y_1, y_2 and r as

$$y_1 = -\frac{\omega_H\omega_L}{\omega_H + \omega_L}\int_0^t x_1(u)du \tag{3.16a}$$

$$y_2 = -\frac{\omega_H\omega_L}{\omega_H + \omega_L}\int_0^t x_2(u)du \tag{3.16b}$$

$$r = \frac{\omega_L\omega_H}{(\omega_L + \omega_H)^2}, \tag{3.16c}$$

we can write our model as

$$y_1' = -rx_1 \tag{3.17a}$$

$$x_1' = -x_1 + y_1 + \beta_1[\alpha_2 \sin^2(x_2(\bar{t} - \bar{\tau_{12}}) + \phi_1) + \sin^2(x_1(\bar{t} - \bar{\tau_{11}}) + \phi_2))] \tag{3.17b}$$

$$y_2' = -rx_2 \tag{3.17c}$$

$$x_2' = -x_2 + y_2 + \beta_2[\alpha_1 \sin^2(x_1(\bar{t} - \bar{\tau_{21}}) + \phi_2) + \sin^2(x_2(\bar{t} - \bar{\tau_{22}}) + \phi_1))]. \tag{3.17d}$$

In this form of the equations governing the dynamics our system, we can observe the symmetry of the solution and give parameters physical significance. The gains in the feedback loops for oscillators 1 and 2 are β_1 and β_2 respectively and the gains in the coupling loops are $\beta_1\alpha_2$ and $\beta_2\alpha_1$. Since in our case we match the two pairs of parameters, these parameters relate to the experimentally measured ones as $\gamma_c = \beta_1\alpha_2 = \beta_2\alpha_1$ and $\gamma_f = \beta_1 = \beta_2$. Similarly, we fix the delay parameters such that $\tau_{11} = \tau_{22} = \tau_f$ and $\tau_{12} = \tau_{21} = \tau_c$. With these changes Eq. (3.17) become

$$y_1' = -rx_1 \tag{3.18a}$$

$$x_1' = -x_1 + y_1 + \gamma_c \sin^2(x_2(\bar{t} - \bar{\tau_c}) + \phi_1) + \gamma_f \sin^2(x_1(\bar{t} - \bar{\tau_f}) + \phi_2)) \tag{3.18b}$$

$$y_2' = -rx_2 \tag{3.18c}$$

$$x_2' = -x_2 + y_2 + \gamma_c \sin^2(x_1(\bar{t} - \bar{\tau_c}) + \phi_2) + \gamma_f \sin^2(x_2(\bar{t} - \bar{\tau_f}) + \phi_1)). \tag{3.18d}$$

These delay differential equations are a good model for our system. By studying symmetries, perturbations about simple solutions and their linear stability, we are able to infer much about the experimental systems they model. As is the case for many nonlinear delay differential equations, the equations cannot be solved analytically in closed form, but they can be solved numerically using an integrator algorithm. The advantage of numerics is that we are able to scan large ranges of parameters without

being limited by experimental concerns. However, it is important to remember that numerics do not exactly model the experiment, since details such as noise, asymmetries, and small parameter deviations cannot be accounted for in our simplified model.

3.3 Verifying the model: Numerical Work

Having developed a model for our system, a natural next step is to test its performance. Numerous previous results have demonstrated its validity [11, 16] when general dynamical behavior is studied. Next, we implement a routine for numerically solving this system.

3.3.1 RADAR5

All numerical simulations presented in this thesis were performed in RADAR5, an implicit Runge-Kutta differential equation solver of order 5. The RADAR5 package is a set of Fortran 90 subroutines developed by Nicola Guglielmi and Ernst Hairer at the University of Geneva. With the help of Lauren Shareshian [11], we have implemented and used the latest version RADAR5 2.1.

The RADAR5 package is designed for solving general initial value problems for delay differential equations of the form

$$\begin{aligned} My'(t) =& f(t, y(t), y\left(\alpha_1(t, y(t))\right), ..., y(\alpha_m(t, y(t)))) \\ y(t_0) =& y_0, \quad y(t) = g(t) \quad \text{for} \quad t < t_0, \end{aligned} \tag{3.19}$$

where M is a constant d $\times$ d matrix and $\alpha_i(t, y(t)) \leq t$ for $t \geq t_0$ for all i. Since matrix M can be singular, the above formulation includes all kinds of differential delay equations. RADAR5 uses collocation methods based on RADAU5 [21] to solve the nonlinear differential equations. The code is versatile and can be adapted to many different kind of problems.

The main quality of RADAR5 is that, when compiled with the Intel provided Fortran compiler iFort, performs very fast integration, allowing us to run simulations over the whole bandwidth of our system[1] in reasonably short real times of tens of seconds.

3.3.2 Simulation Setup

For numerical purposes, the non-dimensional parameters of our system were set to values corresponding to the physical values of the system. To improve the speed of our simulations, we reduced the broadband filtering of our system to the range of 1 MHz - 1 GHz. Since the frequencies of the experimentally observed synchronized dynamics fall well within this range, we expect no major effect of this limitation to the observed dynamics.

[1] This task is very difficult to accomplish with more basic algorithms, as discussed by Greg Hoth in his thesis [16].

Finally, we need to specify an initial state for our system. Since we are not interested in the transient behavior of our system, the exact choice of the initial value is not extremely important. However, in the case of multiple-timescale oscillations, we found that the initial state can "kick" the two oscillators into either in-phase or anti-phase dynamical regimes. The phenomena where several stable asymptotic solutions coexist and the chosen initial conditions determine which solution the system approaches asymptotically is called multistability. Thus, we have implemented a random initial state generator for these cases. By running the code with the same parameters a large number of times (20 in the simulations presented in this thesis), we are able to discern between the cases when the two oscillators always tend towards the same locked solution, either in-phase or out-of-phase and the cases where they "jump" between in-phase and anti-phase behaviors. After computing solutions to the DDEs in Fortran using RADAR5, the data was imported, analyzed and plotted in Octave and MATLAB.

3.4 Numerical Results

We ran our simulations over the parameter ranges of interest. We found it convenient to use $\tau_f = 10$ ns, with τ_c varying from 0.1 ns to 30.0 ns in steps of 0.1 ns, nondimensionalized γ_f=0.6 and γ_c varying from 0.03 to 0.6 in steps of 0.03. For negative round trip gain case, when $\phi_1 = \phi_2 = -\pi/4$, the numerical results are presented in Fig. 3.4.

3.4.1 Negative Round Trip Gain

For the case of negative round-trip gain, when $\phi = -\pi/4$, we measure the natural period associated with the sinusoidal oscillation of the weakly coupled nonlinearities to be $\tau_0 = 20$ ns. The fact that the oscillation period τ_0 is exactly two times the length of the feedback delay τ_f is in accordance with linear stability analysis described by L. Illing and D. J. Gauthier [22]. They show that in the case of negative round-trip gain, stable solutions to the system are found in cases when the oscillatory period is an even multiple of the feedback delay.

As seen in Fig. 3.4, when oscillators are biased at $-\pi/4$, the numerical model reproduces closely the experimental results presented in Figure 2.5. The same horizontal synchronization bands are observed as in the experimental case with multiple-timescale dynamical regions in between. The two nodes oscillate in-phase when the system delays follow the relationship

$$\tau_c/\tau_0 = \frac{2k+1}{2} \qquad \text{(in-phase)}, \tag{3.20}$$

for $k \in \mathbb{Z}$ and anti-phase when the delays follow

$$\tau_c/\tau_0 = k \qquad \text{(anti-phase)}, \tag{3.21}$$

for $k \in \mathbb{Z}$.

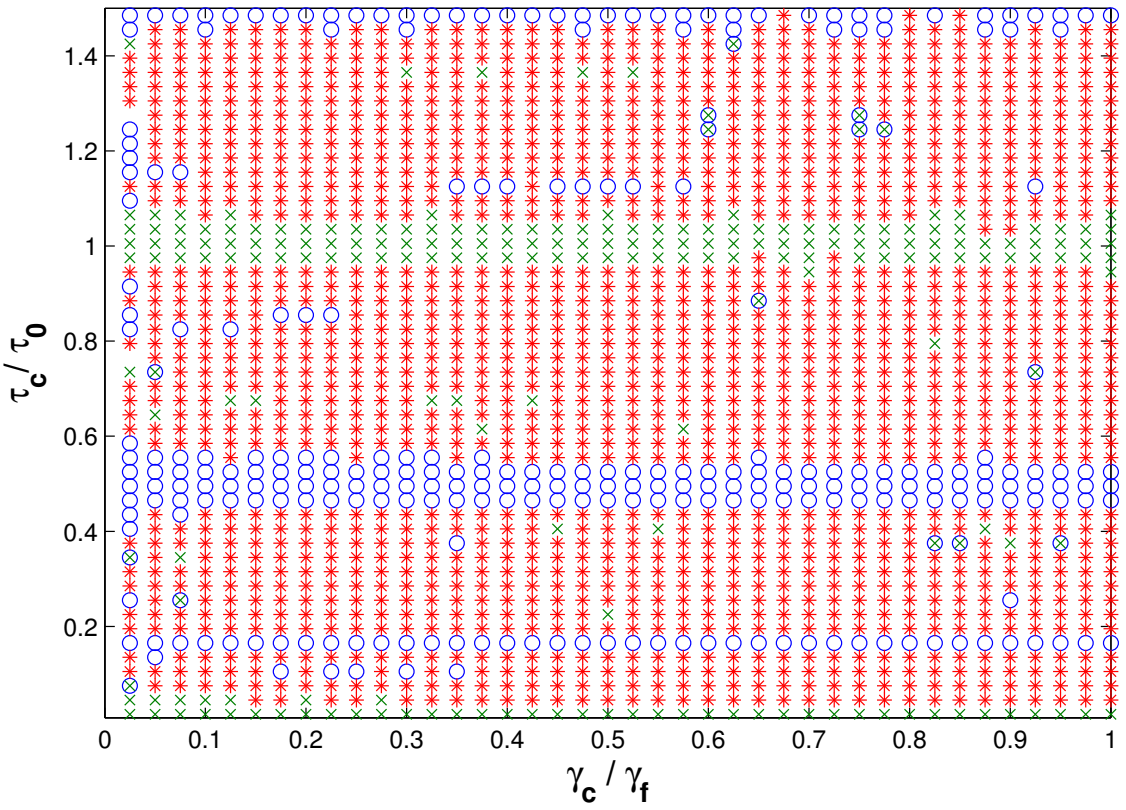

Figure 3.4: Numerics depicting phase locking behavior in parameter space for the case when our oscillators are biased at $-\pi/4$. The two nodes can oscillate in phase ($\bigcirc$), anti phase ($\times$) or in the multiple-timescale regime ($*$). In-phase locking is observed when τ_c/τ_0 is a half-integer and anti-phase locking is observed when τ_c/τ_0 is an integer number.

The outliers in our results can be explained by referring to similar considerations as those discussed in the experimental sections. Depending on the initial condition of the nodes, there are many different attractors in phase space that the two oscillators can end up in. Based on our coordinates in the parameter plot, it is possible that one of the in-phase or anti-phase solutions has a larger basin of attraction than the other, while not necessarily being the only one available. Under these conditions, considering the relatively small number of random initial condition iterations for each data point (20), it is possible that we are missing the other solution for some parameter regions. If this situation occurs, we would record a synchronized solution in the parameter plot, instead of a multi-timescale solution. Another factor that can lead to skewed data is the analysis method used for the raw data output of our numerical integrator. Here, the condition we implement for in-phase or anti-phase synchrony is that the two measured outputs do not differ by more than 1 % at any point. We believe that this condition might be too strict for some cases.

Unlike in the case of experimental results, the two oscillators phase lock even for very low coupling strength ($\gamma_c/\gamma_f < 1\%$). This behavior is explained by the

lack of noise and mismatch, making synchronization possible even for very small coupling strengths. In contrast, the presence of noise and parameter mismatch in the experiment tends to destabilize the phase-locking dynamics of the two oscillators.

3.4.2 Positive Round Trip Gain

For the case when the oscillators are biased at $\pi/4$, the numerical solution method presents several difficulties. Firstly, the large timescale of the slow oscillations observed experimentally requires long integration times and computationally intensive data analysis. Secondly, the solution observed experimentally is hard to simulate numerically, due to the simplified model used for the bandpass filtering. As discussed in Greg Hoth's thesis [16], the experimental broadband filter presents fine characteristics that are not captured in our simplified model. Due to the interplay of these limitations, reaching a numerically stable dynamical regime similar to ones observed experimentally is difficult.

Therefore, while we have observed in-phase locking behavior for $\phi = \pi/4$, in concordance with the experiment, for limited parameter choice, running the simulations over large ranges of values in parameter space is too numerically intensive for the time constraints of this thesis.

Chapter 4

Theory and Insight: Deciphering the Observed Dynamics

In this chapter, we discuss theories that account for the various dynamics observed experimentally and numerically. In the case of negative round trip gain ($\phi = -\pi/4$), the low coupling feedback gain of the system warrants the use of delay-coupled Kuramoto phase oscillators as a simple model that explains the emergence of phase-locking bands in the parameter space. In the case of the positive round trip gain ($\phi = \pi/4$), we argue that the periodic oscillations observed are the result of filtering in our system and that synchronization is always expected in this case.

4.1 Negative round trip gain: A model

4.1.1 Kuramoto oscillators

Since we are discussing the case when our identical oscillators are coupled with low coupling strengths, we expect that the amplitude of the oscillations is unaffected by the weak coupling. Therefore, we can consider the two nodes as individual phase oscillators. A good mathematical model that can offer insight into the dynamical behavior of our system under these conditions is the Kuramoto model. Proposed by Yoshiki Kuramoto in his seminal 1975 paper [23, 24], the model can be a good approximation for several important classes of weakly coupled oscillators [25, 26].

In the Kuramoto model, the dynamics of a general system of delay coupled-phase oscillators is described by:

$$\theta_i'(t) = \omega_{0i} + \frac{K}{k}\sum_{j=1}^{N} A_{ij}\sin[\theta_j(t-\tau_{ij}) - \theta_i(t)], \tag{4.1}$$

where ω_{0i} is the natural frequency of node i, θ_i is the phase variable of node i in the system, K is the coupling strength, i is the index of each oscillator, k is the number of signals each oscillator receives, N is the number of oscillators, τ_{ij} is the delay corresponding to the time-lagged input signal from oscillator j to oscillator i,

and **A** is the adjacency matrix, describing the topology of our network: if oscillator j sends signal to i then $A_{ij} = 1$ and otherwise $A_{ij} = 0$.

4.1.2 A Stability Criterion

For studying the stability of solutions to the Kuramoto equations in the general case, we follow M. Earl and S. Strogatz who offer an elegant solution for general systems of periodic phase oscillators, in the case when each oscillator receives signal from k others [27] and no self-feedback is available. They show that the in-phase solutions are stable if and only if $Kf'(-\Omega\tau) > 0$, where Ω is the collective synchronization frequency. The condition is derived in general form, when the coupling function f is a general well-behaved function.

The derivation starts with the general model

$$\dot{\theta}_i(t) = \omega_0 + \frac{K}{k}\sum_{j=1}^{N} A_{ij} f[\theta_j(t-\tau) - \theta_i(t)], \tag{4.2}$$

where the used parameters are identical to the ones defined above in Eq. (4.1), the only differences being that we replace the sine with the general function f and take the case of matched coupling delays $\tau_{ij} = \tau$ and identical oscillators natural frequency $\omega_{0i} = \omega_0$. We can think of the adjacency matrix A_{ij} as encoding the network topology, since row i represents the connection to oscillator i from oscillator j. Since we have the condition that each oscillator receives signal from k others, each row in this matrix sums to k.

Now, the in-phase synchronized solution is given by

$$\theta_i(t) = \Omega t. \tag{4.3}$$

By substituting Eq. (4.3) in Eq. (4.2), we observe that the synchronization frequency Ω is a solution to equation

$$\Omega = \omega_0 + Kf(-\Omega\tau). \tag{4.4}$$

To perform linear stability analysis, we add a small perturbation to the solutions

$$\theta_i(t) = \Omega t + \epsilon\phi_i(t), \tag{4.5}$$

where $0 < \epsilon \ll 1$. Substituting in the original equation and simplifying, we obtain to first order

$$\dot{\phi}_i(t) = \frac{K}{k} f'(-\Omega\tau)\sum_{j=1}^{N} A_{ij}[\phi_j(t-\tau) - \phi_i(t)]. \tag{4.6}$$

We assume that $Kf'(-\Omega\tau) \neq 0$, condition that allows us to look at the linear term in the perturbation, such that we avoid having to study higher order terms. Now, to study the time behavior of the ϕ variable, we substitute $\phi_i(t) = v_i e^{\lambda t}$ into Eq. (4.6) and obtain

$$v_i \lambda e^{\lambda t} = \frac{K}{k} f'(-\Omega\tau) \sum_{j=1}^{N} A_{ij}[v_j e^{\lambda(t-\tau)} - v_i e^{\lambda t}]. \tag{4.7}$$

Simplifying and massaging the equation gives

$$\sum_{j=1}^{N} A_{ij} v_j = \frac{k e^{\lambda\tau}[\lambda + K f'(-\Omega\tau)]}{K f'(-\Omega\tau)} v_i. \tag{4.8}$$

and we can see that letting

$$\sigma = \frac{k e^{\lambda\tau}[\lambda + K f'(-\Omega\tau)]}{K f'(-\Omega\tau)} \tag{4.9}$$

transforms Eq. (4.8) in an eigenvalue problem, where σ is an eigenvalue of $\mathbf{A}$

$$\mathbf{A}\mathbf{v} = \sigma\mathbf{v}. \tag{4.10}$$

Here $\mathbf{v} = (v_1, ..., v_N)$ is the eigenvector associated with eigenvalue σ. While we cannot calculate the other eigenvalues of matrix $\mathbf{A}$ without knowing more about the structure of $\mathbf{A}$, we can use Gerschgorin's circle theorem [28] to bound their values. The theorem states that every eigenvalue of matrix $\mathbf{A}$ lies in at least one of the circles $C_1, ..., C_n$, where circle C_i has its center at the A_{ii} diagonal entry of matrix $\mathbf{A}$ and its radius is equal to the absolute sum along the rest of the row: $\sum_{j\neq i} |A_{ij}|$. In our case, this means that all of the circles are identical, with center at $a_{ii} = 0$ due to the lack of self-feedback in the system and radius k due to the fact that each oscillator receives signal from other k oscillators. Therefore, the theorem imposes that all of the eigenvalues of matrix $\mathbf{A}$ are within the defined circle and thus satisfy

$$|\sigma| \leq k. \tag{4.11}$$

Now, we can rewrite Eq. (4.9) with $\sigma = |\sigma|e^{i\theta}$, $\beta = (|\sigma|/b)$, with $0 \leq \beta \leq 1$, and $\alpha = K f'(-\Omega\tau)$

$$\alpha\beta e^{i\theta} = e^{\lambda\tau}(\lambda + \alpha). \tag{4.12}$$

For our solutions to exhibit local stability, we require that the real part of our eigenvalues is smaller than zero, i.e. $\mathrm{Re}(\lambda) < 0$.

Proposition 1. For all λ, $\mathrm{Re}(\lambda) < 0$ if and only if $\alpha > 0$.

Now, write λ in the explicit complex form $\lambda = a + ib$ and write Eq. (4.12) in terms of real and imaginary parts to obtain

$$\alpha\beta \cos(\theta - \tau b) e^{-\tau a} = a + \alpha, \tag{4.13}$$

$$\alpha\beta \sin(\theta - \tau b) e^{-\tau a} = b \tag{4.14}$$

If we square and add the two equations, we obtain

$$\alpha^2\beta^2 e^{-2\tau a} = (a + \alpha)^2 + b^2. \tag{4.15}$$

We will show that $\mathrm{Re}(\lambda) = a < 0$ only if $\alpha > 0$ by proving the contrapositive. We assume that $\alpha < 0$ and will prove that there exists at least one solution with $a \geq 0$. Thus, observing that $\rho = -\beta\cos(\theta - \tau b) \in [-1, 1]$ and that $\alpha = -|\alpha|$, we can rewrite Eq. (4.13) as

$$\rho|\alpha|e^{-\tau a} = r - |\alpha|. \tag{4.16}$$

For the case when $\rho \in [0, 1]$, Eq. (4.16) becomes

$$a = (1 + |\rho|e^{-\tau a})|\alpha|. \tag{4.17}$$

It is easy to see that in this case the right hand side is always positive and thus $a > 0$. Now, for the case when $\rho \in [-1, 0)$, Eq. (4.16) is

$$a = (1 - |\rho|e^{-\tau a})|\alpha|. \tag{4.18}$$

When we plot the equation, it is easy to see graphically in Fig. 4.1 that there always exists a solution to Eq. (4.18) with $a > 0$. With this and the previous results in hand, we have proven the direct portion of Proposition 1.

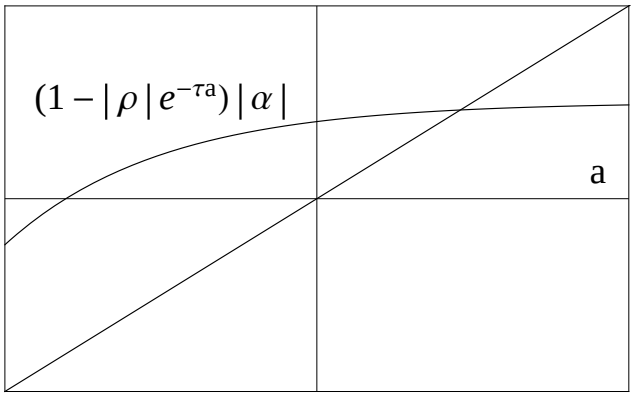

Figure 4.1: Graphical method showing the existence of a solution to Eq. (4.18). We plot variable a on the horizontal axis and the left hand side and right hand side of Eq. (4.18). The intersection points represent solutions to the equation. As we can see, a>0 in this case.

For the reverse direction of Proposition 1 we prove that $a < 0$ if $\alpha > 0$. We assume to the contrary that $\alpha > 0$ and that there exists λ satisfying Eq. (4.12) such that $a \geq 0$. Then $\alpha = |\alpha|$, $a = |a|$ and Eq. (4.15) can be written as

$$\beta^2 e^{-2\tau|a|} = 1 + (a^2 + b^2 + 2|a||\alpha|)/\alpha^2, \tag{4.19}$$

Since $\beta \in [0, 1]$ and $a \geq 0$, the left hand side of the equation $\beta^2 e^{-2\tau|a|} \in [0, 1]$. But the right hand side is greater than or equal to 1 with equality for $a = b = 0$, i.e. $\lambda = 0$. But for $\lambda = 0$, we obtain that $\sigma = k$, with associated eigenvector (1,1,1,...,1). This corresponds to the case when the phase of each oscillator is changed by the same constant amount and reflects the fact that the system is neutrally stable to perturbations of the same constant amount. Since the network is connected, the

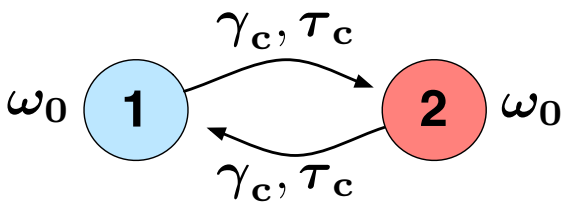

Figure 4.2: Sketch of the simplified system of two coupled oscillators with feedback. Only phase oscillations are considered and the oscillators are considered as oscillating at frequency ω_0, generated by the self-feedback delay τ_f.

eigenspace is one-dimensional [28] and the neutrally stable perturbation is the only solution. For all other perturbations, $\lambda \neq 0$ and we obtain a contradiction between the right side of Eq. (4.19) which is > 1, and and left side of Eq. (4.19) which is ≤ 1. This shows the reverse direction of Proposition 1 and thus completes the proof.

The important results that are obtained from this analysis is that the in-phase solutions are stable if and only if

$$K f'(-\Omega T) > 0. \tag{4.20}$$

4.1.3 Solutions to the Kuramoto equations and stability

We apply the general equations for networks of Kuramoto phase oscillators (Eq. (4.1)) and stability condition (Eq. (4.20)) to our system by using a method first proposed by *D'Huys et al.* [29]. For our system of two coupled nodes with feedback, we can think of the matched feedback delay as introducing an identical natural oscillation frequency $\omega_{01} = \omega_{02} = \omega_0$ for the two oscillators. When uncoupled, both oscillators oscillate with frequency ω_0. We are interested in the phase behavior of the oscillators when they are coupled as shown in Fig. 4.2. Therefore, for our system, the Kuramoto phase equations are

$$\theta_1'(t) = \omega_0 + \frac{K}{2}\sin[\theta_2(t-\tau_c) - \theta_1(t)], \tag{4.21a}$$

$$\theta_2'(t) = \omega_0 + \frac{K}{2}\sin[\theta_1(t-\tau_c) - \theta_2(t)]. \tag{4.21b}$$

Now, we can rescale variables

$$\kappa = \frac{K}{2\omega_0}, \quad T_c = \omega_0\tau_c, \quad t \to \omega_0 t. \tag{4.22}$$

We then have two coupled dimensionless delay-differential equations describing the phase dynamics

$$\dot{\theta}_1 = 1 + \kappa\sin[\theta_2(t-T_c) - \theta_1(t)], \tag{4.23a}$$

$$\dot{\theta}_2 = 1 + \kappa\sin[\theta_1(t-T_c) - \theta_2(t)], \tag{4.23b}$$

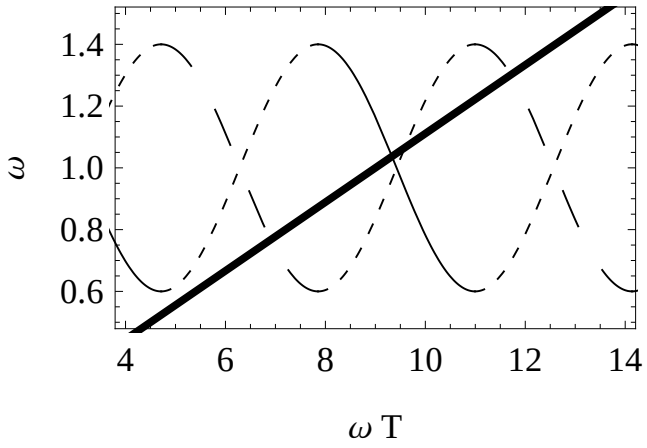

Figure 4.3: Numerical solution of the locking frequencies for the system of two mutually coupled oscillators. Intersections with black curve represent stable in-phase solutions, with dashed curves stable anti-phase states and with dotted lines unstable frequencies. The parameters used to obtain the plot were $\kappa = -0.4$ and $T_c = 9$.

where the dot denotes the derivative with respect to the nondimensionalized time.

Due to the delay coupling, multiple solutions with different locking frequencies are possible. For the in-phase solutions: $\theta_1(t) = \theta_2(t) = \omega t$. Then the system of equations reduces to solving

$$\omega = 1 - \kappa \sin(\omega T_c). \tag{4.24}$$

For the anti-phase solutions we have $\theta_1(t) = \theta_2(t) + \pi = \omega t$. Plugging into Eq. (4.23), we obtain

$$\omega = 1 + \kappa \sin(\omega T_c). \tag{4.25}$$

Applying the stability condition derived in Eq. (4.20) to our system, we have that $\Omega = \omega_0 \omega$ and f is the sine function. The stability criterion shows that the in-phase solution is stable if and only if

$$\kappa \cos(\omega \tau_c) > 0. \tag{4.26}$$

Analogously, we see that for the anti-phase solution the sign of κ changes. Therefore, the anti-phase solution is stable if and only if

$$\kappa \cos(\omega \tau_c) < 0. \tag{4.27}$$

For given parameters κ and T_c, we can easily obtain numerical solutions to these equations. Figure 4.3 depicts a graphical method of solving these nonlinear equations. Here, we plot the left hand side of Eq. (4.24) and Eq. (4.25) with a black thick line, the right hand side of Eq. (4.24) with a full black curve in the stable region and the right hand side of Eq. (4.25) with a dashed curve. The unstable regions for both equations are represented by dotted lines. Therefore, the graphical intersection of the thick line with the full black line represents stable in-phase solutions, the intersection of the thick line with the dashed curve represents stable anti-phase solutions and the intersection of the thick line with the dotted line represents unstable solutions.

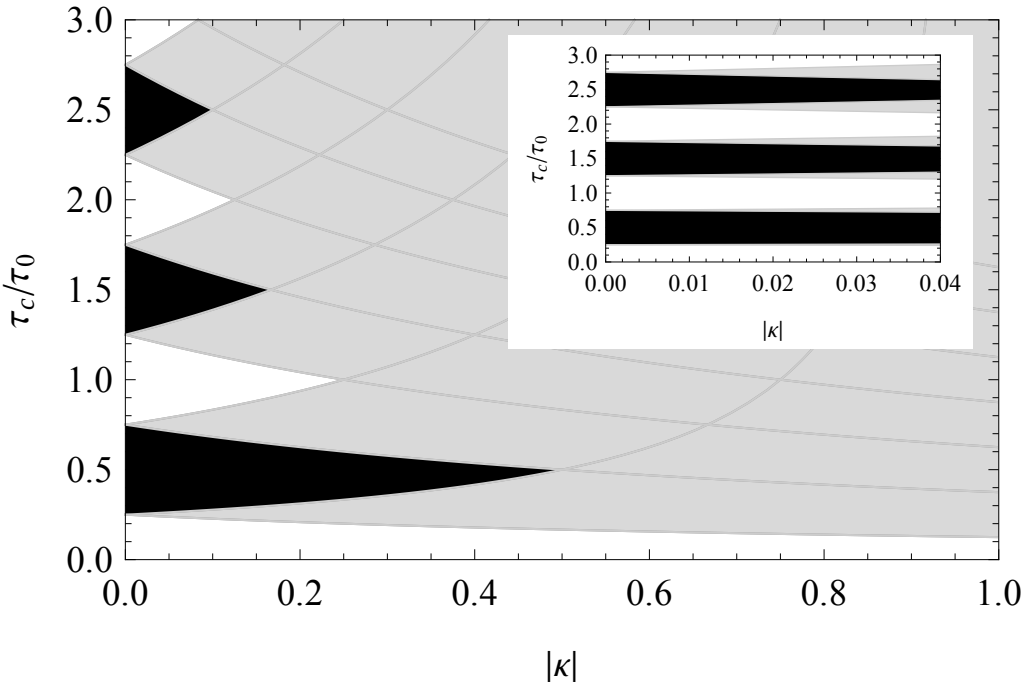

Figure 4.4: Stable regions in parameter space for the coupled Kuramoto phase oscillators. The coupling is repulsive $\kappa < 0$, consistent with the $\phi = -\pi/4$ negative round trip gain regime. The plot displays stable in-phase solutions (black), stable anti-phase solutions (white) and multistability, when the two states coexist (gray). (Inset) The same stability regions plotted for small coupling feedback. We observe stable in-phase bands at half-integer τ_c/τ_0 values and anti-phase bands at integer τ_c/τ_0 values.

4.1.4 Back to Parameter Space

The solutions of Eq. (4.24) are Eq. (4.25) are plotted in in parameter space, together with the regions where they are stable or unstable given by the stability conditions in Eq. (4.26) and Eq. (4.27). The results of this analysis are summarized in Fig. 4.4, where the delay axis has been rescaled to represent the ratio of coupling delay to the natural period τ_c/τ_0, where $\tau_0 = 2\pi/\omega_0$. Stable in-phase solutions are shown in black, stable anti-phase solutions are shown in white and regions of multistability, where the two states coexist, are shown in gray. As we can observe in the inset of the figure, for low coupling $\kappa \ll 1$, the theory predicts the occurrence of locked in-phase oscillation bands at half-integer values of the ratio of coupling delay to natural delay τ_c/τ_0, locked anti-phase oscillation bands at integer values of τ_c/τ_0 and the existence of multistability in the intermediate regions. This is the same behavior we have observed in the experimental and numerical analysis in Fig. 2.5 and Fig. 3.4 respectively, where the multi-timescale dynamics correspond to multistability for phase oscillations.

A careful inspection of Fig. 4.4 shows that, even in the case of very weak coupling, there are noticeable differences between the numerically and experimentally

observed dynamics and our theory. Theory predicts that the width of the synchronization regions varies significantly with gain, variations that are not reflected in our experimental and numerical results. While the Kuramoto phase model accounts for the observed phase dynamics in our system, the effects of amplitude oscillations are completely ignored. Therefore, the task of mapping our coupling strength factor γ_c in our DDE model in Eq. (3.18) to the Kuramoto coupling factor K is a daunting task. Without this important correspondence, the effect of varying coupling strengths on the phase locking dynamics on our system is impossible to characterize. However, since this thesis focuses on the the role of delay in such systems, the fact that we are observing the same bands of phase-locked dynamics and multistability as in the experiment and numerics is enough to warrant the practicality of this model.

4.2 Positive round trip gain

As observed experimentally and numerically, the case when the oscillators are biased at $\phi = \pi/4$, resulting in a positive round trip gain, is distinct from the negative round trip gain case. Experimentally, we observe oscillations on a very slow timescale with a frequency of 217 KHz, corresponding to a period that is 80 times larger the feedback delay. In this case, we have always observed in-phase locking for strong enough coupling ($\gamma_c/\gamma_f > 10\%$). These results suggest that, for low coupling, the oscillations are not the result of the destabilizing effect of the feedback delay. As suggested by Peil et al. [17], the slow timescale dynamics are internally generated by system dynamics with an oscillation period related to the timescale of the high pass filtering in the system, $1/\omega_L$.

To analyze these results, we again employ the Kuramoto model for phase oscillators. Since the dynamics are on a timescale that is two orders of magnitude larger than the coupling delay τ_c, we can neglect the delay. The Kuramoto equations become

$$\theta_1'(t) = \omega_0 + \frac{K}{2}\sin[\theta_2(t) - \theta_1(t)], \tag{4.28a}$$

$$\theta_2'(t) = \omega_0 + \frac{K}{2}\sin[\theta_1(t) - \theta_2(t)]. \tag{4.28b}$$

Now, if we let $\Delta(t) = \theta_1(t) - \theta_2(t)$ and take the difference of Eq. (4.28a) and (4.28b) we obtain

$$\Delta'(t) = -K\sin[\Delta(t)], \tag{4.29}$$

where Δ is defined on $[0, 2\pi]$. The solution to Eq. (4.29) is just

$$\Delta(t) = \arctan(e^{-Kt}). \tag{4.30}$$

It is now clear that for large t, $\Delta \to 0$ and the long time behavior is for the two oscillators to exhibit in-phase synchronization, as observed experimentally.

Another, perhaps more intuitive solution is presented graphically in Fig. 4.5. Here, we have plotted the phase difference Δ on the horizontal axis and the instantaneous

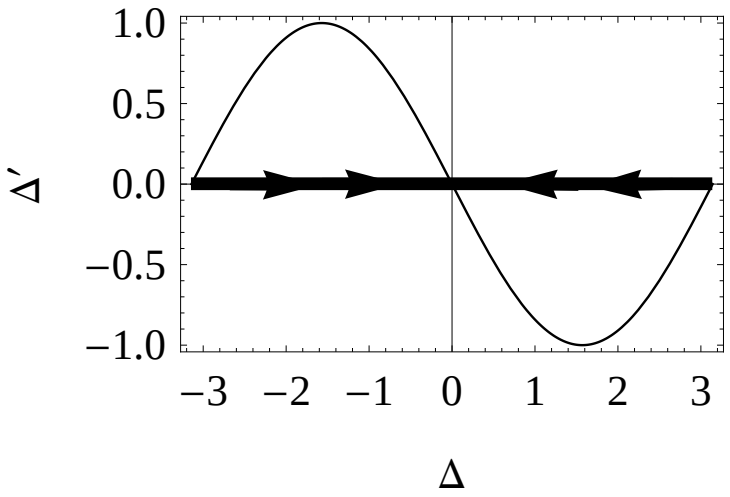

Figure 4.5: Plot showing the time evolution of parameter Δ. Time evolution of phase difference Δ' is plotted on the vertical axis and phase difference Δ is plotted on the horizontal axis. As shown by the arrows, the system always tends towards the synchronized solution $\Delta = 0$.

change in phase difference Δ' on the vertical axis. For the case when $\Delta > 0$, the slope of the Δ function is negative, i.e. $\Delta' < 0$, and so the phase difference decreases in time until $\Delta' = 0$, such that $\Delta \to 0$ for large t. Similarly, for the case when $\Delta < 0$, the slope of the Δ function is positive, i.e. $\Delta' > 0$, and so the phase difference increases in time until $\Delta' = 0$, such that $\Delta \to 0$ for large t. Therefore, the long-term behavior of the two systems is always to oscillate in-phase.

In conclusion, both methods explain the observed experimental and numerical phase-locking behavior in the case when the nonlinearity is biased at $\pi/4$, where the two oscillators always synchronize in-phase.

Conclusion

In this thesis, we have shown through experiments, numerics, and analytic methods that synchronization of two weakly coupled optoelectronic oscillators with unequal delay can be achieved for sufficiently strong coupling. In the regime close to the oscillation onset and with the nonlinearities biased at -$\pi/4$, we observed in-phase oscillations when the coupling delay τ_c is a half-integer multiple of the period τ_0 associated with the natural oscillations arising in the system and anti-phase oscillations when the coupling delay τ_c is an integer multiple of the natural delay τ_0. When biased at $\pi/4$, the two nonlinearities are always observed to oscillate in-phase. For very weak coupling, the system exhibits phase slipping behavior.

The results of this thesis have significance in the larger picture of studying network dynamics. We show that synchronization is possible in the case of unequal coupling delays and determine the conditions under which synchronization occurs and characterize its properties. These results have possible practical applications in many fields studying complex systems such as communications, neuroscience or group dynamics.

While successful in observing consistent results for the synchronization dynamics of our system experimentally, numerically and analytically, there are a few details of this work that need further work. For example, we would like to obtain a rigorous numerical analysis of our system for the case of positive round trip gain and also ensure that all our simulations are performed at parameters corresponding to the experimental setup. Such a result would require higher computational power and optimization of the algorithms used.

On the theoretical analysis side, we would like to develop a model that includes amplitude oscillations and try to generalize our results to more complex networks of many coupled optoelectronic oscillators. Finally, we hope that the insight gained from studying phase-locking dynamics in the periodic oscillations regime will help us understand and analyze more complex dynamical regimes, such as chaos, for the case of varying delays.

References

[1] C. Masoller, M. Torrent, and J. García-Ojalvo, "Interplay of subthreshold activity, time-delayed feedback, and noise on neuronal firing patterns," Phys. Rev. E **78** (2008).

[2] P. R. Roelfsema, A. K. Engel, Peter König, and W. Singer, "Visoumotor integration is associated with zero time-lag syncrhonization among cortical areas," Nature **385**, 157 (1997).

[3] G. Kozyreff, A. Vladimirov, and P. Mandel, "Global Coupling with Time Delay in an Array of Semiconductor Lasers," Phys. Rev. Lett. **85**, 3809–3812 (2000).

[4] M. Kim, R. Roy, J. Aron, T. Carr, and I. Schwartz, "Scaling Behavior of Laser Population Dynamics with Time-Delayed Coupling: Theory and Experiment," Phys. Rev. Lett. **94** (2005).

[5] I. Fischer, R. Vicente, J. Buldú, M. Peil, C. Mirasso, M. Torrent, and J. García-Ojalvo, "Zero-Lag Long-Range Synchronization via Dynamical Relaying," Phys. Rev. Lett. **97** (2006).

[6] M. Peil, L. Larger, and I. Fischer, "Versatile and robust chaos synchronization phenomena imposed by delayed shared feedback coupling," Phys. Rev. E **76** (2007).

[7] A. Argyris, D. Syvridis, L. Larger, V. Annovazzi-Lodi, P. Colet, I. Fischer, J. García-Ojalvo, C. R. Mirasso, L. Pesquera, and K. A. Shore, "Chaos-based communications at high bit rates using commercial fibre-optic links," Nature **438**, 343–6 (2005).

[8] C. J. May, Undergraduate thesis, Reed College (2008).

[9] I. Kanter, E. Kopelowitz, and W. Kinzel, "Public Channel Cryptography: Chaos Synchronization and Hilberts Tenth Problem," Phys. Rev. Lett. **101** (2008).

[10] A. Uchida, K. Amano, M. Inoue, K. Hirano, S. Naito, H. Someya, I. Oowada, T. Kurashige, M. Shiki, S. Yoshimori, et al., "Fast physical random bit generation with chaotic semiconductor lasers," Nature Photonics **2**, 728–732 (2008).

[11] L. Illing, C. Panda, and L. Shareshian, "Isochronal chaos synchronization of delay-coupled optoelectronic oscillators," Phys. Rev. E **84** (2011).

[12] A. Englert, W. Kinzel, Y. Aviad, M. Butkovski, I. Reidler, M. Zigzag, I. Kanter, and M. Rosenbluh, "Zero Lag Synchronization of Chaotic Systems with Time Delayed Couplings," Phys. Rev. Lett. **104** (2010).

[13] M. Zigzag, M. Butkovski, A. Englert, W. Kinzel, and I. Kanter, "Zero-lag synchronization and multiple time delays in two coupled chaotic systems," Phys. Rev. E **81** (2010).

[14] D. J. Griffiths, *Introduction to Electrodynamics* (Prentice Hall, New Jersey, 1999), 3rd ed.

[15] C. Edward, *Polarized Light in Fiber Optics* (Polawave Group, Lincroft, 2003).

[16] G. Hoth, Undergraduate thesis, Reed College (2010).

[17] M. Peil, M. Jacquot, Y. Chembo, L. Larger, and T. Erneux, "Routes to chaos and multiple time scale dynamics in broadband bandpass nonlinear delay electro-optic oscillators," Phys. Rev. E **79** (2009).

[18] Y. Chembo Kouomou, P. Colet, L. Larger, and N. Gastaud, "Chaotic Breathers in Delayed Electro-Optical Systems," Phys. Rev. Lett. **95** (2005).

[19] L. Illing, G. Hoth, L. Shareshian, and C. May, "Scaling behavior of oscillations arising in delay-coupled optoelectronic oscillators," Phys. Rev. E **83** (2011).

[20] K. E. Callan, L. Illing, Z. Gao, D. J. Gauthier, and E. Schöll, "Broadband Chaos Generated by an Optoelectronic Oscillator," Phys. Rev. Lett. **104** (2010).

[21] E. Hairer and G. Wanner, *Solving Ordinary Differential Equations II: Stiff and Differential-Algebraic Problems* (Springer, New York, 2004).

[22] L. Illing and D. J. Gauthier, "Hopf bifurcations in time-delay systems with band-limited feedback," Physica D **210**, 180–202 (2005).

[23] Y. Kuramoto, *International Symposium on Mathematical Problems in Theoretical Physics, Lecture Notes in Physics* (Springer, New York, 1975).

[24] Y. Kuramoto, *Chemical oscillations, waves, and turbulence* (Dover Publications, New York, 2003).

[25] Y. Kuramoto, "Phase- and Center-Manifold Reductions for Large Populations of Coupled Oscillators with Application to Non-Locally Coupled Systems," Int. J. Bifurcation Chaos Appl. Sci. Eng. **7**, 789 (1997).

[26] H. Daido, "Order Function Theory of Macroscopic Phase-Locking in Globally and Weakly Coupled Limit-Cycle Oscillators," Int. J. Bifurcation Chaos Appl. Sci. Eng. **7**, 807 (1997).

[27] M. Earl and S. Strogatz, "Synchronization in oscillator networks with delayed coupling: A stability criterion," Phys. Rev. E **67** (2003).

[28] G. Strang, *Introduction to Applied Mathematics*, vol. 69 (Wellesley-Cambridge Press, Wellesley, 1986).

[29] O. D'Huys, R. Vicente, T. Erneux, J. Danckaert, and I. Fischer, "Synchronization properties of network motifs: influence of coupling delay and symmetry," Chaos **18**, 037116 (2008).